

Gyroscope Calibration and Dead Reckoning for an Autonomous Underwater Vehicle

Aaron J Kapaldo

Thesis submitted to the Faculty of the
Virginia Polytechnic Institute and State University
in partial fulfillment of the requirements for the degree of

Masters of Science
in
Electrical Engineering

Daniel J. Stilwell, Chair

William T. Baumann, Member

Pushkin Kachroo, Member

July 28, 2005
Blacksburg, Virginia

Keywords: Inertial Navigation, Adaptive Filtering, Dead Reckoning, Extended Kalman Filter

Copyright 2005, Aaron J. Kapaldo

Gyroscope Calibration and Dead Reckoning for an Autonomous Underwater Vehicle

Aaron J Kapaldo

ABSTRACT

Autonomous Underwater Vehicles (AUVs) are currently being used for many underwater tasks such as mapping underwater terrain, detection of underwater objects, and assessment of water quality. Possible uses continue to grow as the vehicles become smaller, more agile, and less expensive to operate. However, trade-offs exist between making less expensive, miniature AUVs and the quality at which they perform. One area affected by cost and size is the onboard navigation system. To achieve the challenges of low-cost rate sensors, this thesis examines calibration methods that are suitable for identifying calibration coefficients in low-cost MEMS gyros.

A brief introduction to underwater navigation is presented and is followed by the development of a model to describe the operation of a rate gyro. The model uses the integral relationship between angular rate and angular position measurements. A compass and two tilt sensors provide calibrated angular position data against which the three single axis gyros are compared to obtain an error signal describing errors present in the angular rate measurements.

A calibration routine that adaptively identifies error parameters in the gyros is developed. Update laws are chosen to recursively apply estimated error parameters to minimize the system error signal. Finally, this calibration method is applied to a simple dead reckoning algorithm in an attempt to measure the improvements calibration provides.

Acknowledgements

I would like to thank my advisor, Dr. Stilwell, for his time and patience with me throughout the course of my graduate degree program. Without his constant support and encouragement, this thesis would not have been possible. Whenever there was problem I couldn't work though, he was always there to give helpful advice or another point-of-view. Thanks also go to my committee members, Dr. Baumann and Dr. Kachroo, for their excellent teaching and support.

Thanks to everyone in the lab: Chris for his always positive attitude and ability to answer any question and Gray for his patience during the long hours discussing Real Analysis homework problems. Jan for the enormous assistance in building all the AUVs and Aditya for all his help in diagnosing AUV problems in the middle of Claytor Lake. Finally, thanks go to Ryan for the time spent discussing dead reckoning and for his excellent programming skills.

Contents

- 1 Introduction** **1**
 - 1.1 Motivation 1
 - 1.2 Review of Dead Reckoning 2
 - 1.3 Previous Work 3
 - 1.4 The ASCL AUV 4
 - 1.5 Thesis Outline 4

- 2 Rate Gyroscope** **6**
 - 2.1 Gyroscope Operation 6
 - 2.2 Modeling Gyroscope Performance 7
 - 2.2.1 Identifying Gyroscope Errors 7
 - 2.2.2 Defining Coordinate Mappings 8

2.2.3	Derivation of Gyroscope Model	9
3	Gyroscope Calibration	13
3.1	Motivation	13
3.2	Adaptive Parameter Identification	17
3.2.1	Defining Parameter Update Functions	19
3.2.2	Lyapunov Stability Analysis	22
3.2.3	Simulation of Adaptive Identifier	23
3.3	Adaptive Identifier Performance on Real Data	36
3.3.1	Calibration Considerations	41
4	Dead Reckoning	43
4.1	Extended Kalman Filter	43
4.1.1	Problem Setup	43
4.2	Applying the Extended Kalman Filter	45
4.3	Results	46
4.4	Gyro Calibration Effects on Dead Reckoning	48

5	Conclusions and Future Work	51
5.1	Conclusions	51
5.2	Future Work	52

List of Figures

2.1	Body fixed coordinate system used to describe angular motion in the body frame,[7].	8
2.2	Angular position represented in local-level frame,[7].	9
3.1	Path trajectories for simulation of gyroscope calibration.	25
3.2	Adaptive identifier simulation, path 2.	26
3.3	Adaptive identifier simulation, path 3.	27
3.4	Adaptive identifier simulation, path 5.	28
3.5	Adaptive identifier simulation, path 7.	29
3.6	Adaptive identifier simulation, path 2 convergence.	30
3.7	Adaptive identifier simulation, path 3 convergence.	31
3.8	Adaptive identifier simulation, path 5 convergence.	32

3.9	Adaptive identifier simulation, path 7 convergence.	33
3.10	Straight-line trajectory sensor data.	37
3.11	Straight-line parameter convergence.	38
3.12	Square trajectory sensor data.	39
3.13	Square parameter convergence.	40
4.1	Dead Reckoning of the straight-line and square trajectories.	47
4.2	Comparison of calibrated vs. uncalibrated gyro on the dead reckoned position for straight-line trajectory.	48
4.3	Comparison of calibrated vs. uncalibrated gyro on the dead reckoned position for square trajectory.	49

List of Tables

1.1	Specifications of the ASCL AUV IMU	5
3.1	Simulation settings.	24
3.2	Adaptive identifier simulation results, X gyroscope.	34
3.3	Adaptive identifier simulation results, Y gyroscope.	35
3.4	Adaptive identifier simulation results, Z gyroscope.	35
3.5	Commands for straight-line trajectory.	36
3.6	Commands for square trajectory.	41

Chapter 1

Introduction

1.1 Motivation

Autonomous Underwater Vehicles (AUVs) are devices that perform tasks with little or no human interaction. In general, these tasks, a predefined set of commands, achieve a desired mission goal when completed. By operating autonomously, outside control is removed from the control loop and the AUV monitors and processes its own onboard sensors to determine the efficiency with which each command is being accomplished. Decisions by the AUV are made based on operating guidelines that have been programmed into the vehicle control system.

Currently, AUV technology is being utilized by the military to perform operations that are too dangerous for direct human interaction, such as the detection of mine-like objects. Scientists also have a vested interest in AUV development to perform ecological studies and to map lakes, rivers, and oceans, among many other applications, [6]. The development of AUVs for aquatic research is a growing field with platforms generally being developed for one

of two categories. The first category involves developing an AUV capable of performing long range missions for large scale mapping and monitoring. The second category involves the development of smaller or miniature AUVs to monitor and measure more localized processes with a higher resolution than can be obtained by a larger AUV.

AUVs must possess capabilities to follow a desired course accurately. For most missions, the vehicle position must be known at all times to georeference data collected by the AUV. One example of such a mission is the tracking and mapping of a fresh water outflow entering a coastal environment via a drainage pipe from shore using inertial navigation. Assume that the AUV has knowledge of its initial attitude and position in the navigation frame. Assume also that there exists a constant offset, ψ , in the heading sensor measurement. This offset error will be present throughout the entire run causing the vehicle trajectory to be rotated about the initial position by an angle of ψ . The scenario is further complicated by the introduction of time-varying measurement drift commonly seen in navigation sensors. The longer the AUV runs, the greater the difference between the measured and true positions. This example illustrates the need to keep all navigation sensors properly calibrated.

1.2 Review of Dead Reckoning

When navigating underwater, GPS is not available and the absolute position of the vehicle is unknown. Dead reckoning, a method of navigation that uses on-board sensors to measure speed and heading based on the last known position to estimate its current position, [2], becomes important. The last GPS fix received before the AUV dives becomes the initial condition for a dead reckoning algorithm. Onboard sensors, gyroscopes and a compass, provide vehicle attitude and orientation information. Speed is either measured in real time or is determined empirically through testing. When accelerometers are available onboard, a more advanced form of dead reckoning known as inertial navigation is possible. Inertial

navigation integrates accelerations and rotation rates of a body in time to determine attitude and heading. Since the ASCL AUV does not have onboard accelerometers, this form of dead reckoning will not be examined in this thesis.

Errors in dead reckoning result from many sources, including inaccurate knowledge of the vehicle's starting position, a misalignment of the heading sensor, and the time-varying effects of the sensors. Any errors present in the initial conditions will be propagated throughout the vehicle run. Similarly, a misaligned compass causes a constant offset in all measurements and translates over time into an estimated heading trajectory that deviates from the actual vehicle trajectory. Finally, the constant drift in gyroscopes becomes significant with time.

1.3 Previous Work

Research has shown that with accurate pre-flight calibration, dead reckoning is able to accurately calculate vehicle position for short periods of time, [9]. While the vehicle is at rest, biases in accelerometers and gyroscopes can be obtained using measurements from the inertial measurement unit as well as tilt and heading sensors. Once initial biases are known, inertial navigation is possible for short periods of time before absolute positioning is required to reset system error near zero.

When longer mission times are required, the drift characteristics of the sensors make it necessary for position corrections to be introduced into the system from external sensors such as GPS when on the surface or from an acoustic positioning system when underwater. In [3], the authors showed this when they implemented an online extended Kalman filter (EKF) that fused data from a low-frequency long-base-line acoustic positioning system and a Doppler sonar system with a gyroscope and compass error model. Corrections from the low-frequency sensors allowed the EKF to recursively estimate the bias parameters of the

gyroscopes and compass.

The authors in [5], show that when space allows, larger sensors such as highly accurate precision gyrocompasses and bottom lock Doppler sonar can be installed. The calibration question then becomes how to align these sensors to correlate their measurements not only with the vehicle frame but also with each other. The authors proposed a least-squares algorithm to estimate the rotational misalignment between the sensors. The method utilized singular value decomposition methods to calculate the rotation matrices. Navigation performance was shown to be greatly improved with the accurate knowledge of sensor placements in the AUV.

1.4 The ASCL AUV

The ASCL AUV's inertial measurement unit (IMU) uses a commercial compass and a custom-made sensor board. Three single axis gyroscopes are mounted on a circuit board that aligns each gyro with an axis of rotation. A three-axis magnetometer and dual-axis electrolytic inclinometer are part of the commercial-off-the-shelf (COTS) magnetic compass made by True North Technologies (TNT). Table 1.1 gives specific information regarding the performance of each sensor. Also available when the AUV is on the surface is a GPS receiver for absolute position measurements.

1.5 Thesis Outline

This thesis examines in detail the steps required to calibrate and maintain gyro measurements. The TNT compass comes with a calibration routine that can be performed before

Table 1.1: Specifications of the ASCL AUV IMU

Angular Rate	Performance: $\pm 150^\circ/sec$ Resolution: $0.005^\circ/sec$
Magnetic Heading	Accuracy: $< 0.5^\circ$
Pitch and Roll	Performance $\pm 40^\circ$ Tilt Acc.: $< 0.2^\circ$
Absolute Position	Accuracy: $< 10 meters$

operating the vehicle. Therefore, this thesis assumes that the compass is calibrated and all measurements are reliable. In Chapter 2, a system model will be developed to describe the operation of the gyroscopes. Errors specific to gyro operation will also be modeled. In Chapter 3, the developed model will be used to derive an online calibration algorithm to identify and correct for errors in the gyro output. The algorithm is tested on simulated and real data to analyze its performance. Once the data from the AUV is calibrated, Chapter 4 presents a Kalman Filter based dead reckoning algorithm, which is used to further explore the benefits of calibrated gyro measurements. Finally, Chapter 5 will conclude the thesis with observations on the performance of the dead reckoning algorithm and propose key steps to be taken to further develop the inertial navigation system for the ASCL AUV.

Chapter 2

Rate Gyroscope

The rate gyroscope is a key element of a dead reckoning system. The integral relationship between angular rate and angular position forms the basic building block upon which a dead reckoning algorithm estimates vehicle position. This chapter examines the basic operation of a rate gyro and derives a system model based on the integral relationship between compass and gyro to characterize its performance errors.

2.1 Gyroscope Operation

The ASCL AUV is equipped with three strap-down, single-axis resonator gyroscopes from Analog Devices. Resonating or vibratory gyroscopes are characterized by their quick reaction times and, due to the few moving parts, are generally referred to as solid-state sensors. In place of a spinning mass common in many gyros, vibratory gyroscopes operate using two electrostatically driven resonating structures. The velocity created by the vibrating frames allows a Coriolis force to be induced in the presence of an angular velocity, which is then

sensed and converted to an output voltage proportional to the angular velocity, [1].

2.2 Modeling Gyroscope Performance

2.2.1 Identifying Gyroscope Errors

The output signal of a gyro is written as

$$\omega_m(t) = (1 + a)\omega(t) + b \quad (2.1)$$

where the measured angular rate, $\omega_m(t)$, is expressed in terms of the true angular rate, $\omega(t)$, and two unknown constants, a and b , which represent a scaling and a biasing of the output, respectively. In the measured output, bias is caused by changes in temperature, magnetic fields, and also by residual moments in the sensor itself. The level of excitation or acceleration of the sensor does not affect the bias, however. Scaling results from changes in temperature, and non-linearities affecting the ratio of output force to input force.

In addition to these error sources, there are also errors that must be modeled stochastically as a zero-mean random bias caused by instabilities in the sensor performance. Variations in sensor movements such as jitter in the sensor or vehicle frame can cause the output reading to randomly drift with time. Since this error is not constant, it is very difficult to calibrate out, [14]. For simplicity, all errors in bias and scaling are lumped together into two separate error parameters. Rewriting (2.1) in terms of the measured angular rate is more convenient.

$$\omega(t) = \bar{a}\omega_m(t) + \bar{b} \quad (2.2)$$

with

$$\bar{a} = \frac{1}{1 + a}, \quad \text{and} \quad \bar{b} = \frac{-b}{1 + a}.$$

Using (2.2) to express the gyroscope errors for the roll, pitch, and yaw body-coordinate axis, ϕ, θ, ψ , respectively, yields a set of equations describing the gyroscope system as a whole.

$$\begin{bmatrix} \omega_\phi(t) \\ \omega_\theta(t) \\ \omega_\psi(t) \end{bmatrix} = \begin{bmatrix} \bar{a}_\phi & 0 & 0 \\ 0 & \bar{a}_\theta & 0 \\ 0 & 0 & \bar{a}_\psi \end{bmatrix} \begin{bmatrix} \omega_{\phi,m}(t) \\ \omega_{\theta,m}(t) \\ \omega_{\psi,m}(t) \end{bmatrix} + \begin{bmatrix} \bar{b}_\phi \\ \bar{b}_\theta \\ \bar{b}_\psi \end{bmatrix} \quad (2.3)$$

2.2.2 Defining Coordinate Mappings

Figure (2.1) shows a diagram of the AUV body-fixed coordinate system, which will be used to describe localized angular movements of the vehicle. A second coordinate frame, referred

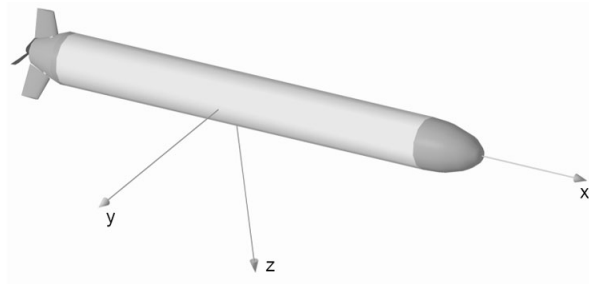


Figure 2.1: Body fixed coordinate system used to describe angular motion in the body frame,[7].

to here as the local-level or navigation frame, has its origin coincident to the body-fixed frame: the positive z-axis points in the direction of the gravity vector and the x- and y-axes point North and East, respectively. A frame in this orientation is often referred to as the North-East-Down (NED) coordinate system. The angular position of the AUV is measured using Euler angles referenced to the local-level coordinate system. Figure (2.2) gives an illustration of these angles. Since the compass and gyros output measurements are referenced to different coordinate frames, the model derived relating gyro and compass measurements must include a transformation from the body-frame to the navigation-frame.

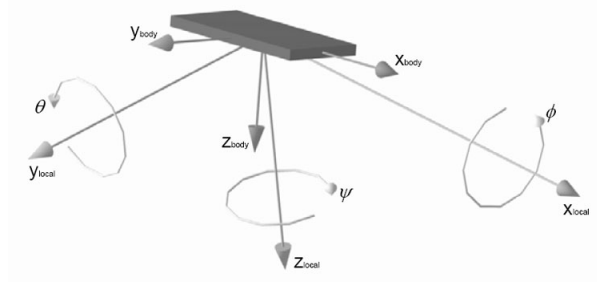


Figure 2.2: Angular position represented in local-level frame,[7].

2.2.3 Derivation of Gyroscope Model

A compass exhibits long-term measurement stability, while a gyro is accurate over short time periods. By comparing the two measurements in time, the error between them will in some form describe the scale and bias errors inherent to the angular rate measurements.

The angular displacement of a rigid body with respect to the navigation-frame is expressed using the Euler angles, ϕ , θ , ψ , representing roll, pitch, and yaw, respectively. To simplify the notation, we will denote the vector of Euler angles by

$$\eta = [\phi, \theta, \psi]^T \in \mathbb{R}^3 \quad (2.4)$$

Body-fixed angular rates of a rigid body AUV, as measured by the gyros, are expressed as

$$\omega(t) = [\omega_\phi(t), \omega_\theta(t), \omega_\psi(t)]^T \in \mathbb{R}^3. \quad (2.5)$$

Integration of these angular rates does not yield physically meaningful angular displacements since they cannot be directly compared to navigation-frame Euler angles. This issue can be resolved by applying a mapping from body-fixed coordinates to navigation coordinates defined by the proper rotation matrix, $R(\eta(t)) : \mathbb{R}^3 \rightarrow SO(3)$ where $R(\eta(t))$ is defined by the product of three successive rotations, [13].

$$R_B^N(\eta(t)) = R_x(\phi(t))R_y(\theta(t))R_z(\psi(t)), \quad (2.6)$$

where

$$R_x(\phi(t)) = \begin{bmatrix} 1 & 0 & 0 \\ 0 & \cos \phi(t) & \sin \phi(t) \\ 0 & -\sin \phi(t) & \cos \phi(t) \end{bmatrix} \quad (2.7)$$

$$R_y(\theta(t)) = \begin{bmatrix} \cos \theta(t) & 0 & -\sin \theta(t) \\ 0 & 1 & 0 \\ \sin \theta(t) & 0 & \cos \theta(t) \end{bmatrix} \quad (2.8)$$

$$R_z(\psi(t)) = \begin{bmatrix} \cos \psi(t) & \sin \psi(t) & 0 \\ -\sin \psi(t) & \cos \psi(t) & 0 \\ 0 & 0 & 1 \end{bmatrix} \quad (2.9)$$

and $R_x(\phi(t)) \in SO(3)$ is the rotation about the x-axis by $\phi(t)$, $R_y(\theta(t)) \in SO(3)$ is the rotation about the y-axis by $\theta(t)$, and $R_z(\psi(t)) \in SO(3)$ is the rotation about the z-axis by $\psi(t)$. The superscript, N , and subscript, B in (2.6) signify the transformation from the navigation coordinate frame to the body-fixed coordinate frame. The time derivative of (2.6) is taken,

$$\dot{R}(\eta(t)) = S(\omega(t))R(\eta(t)), \quad (2.10)$$

where $S(\omega(t)) : \mathbb{R}^3 \rightarrow SS(3)$ is the skew symmetric matrix function.

$$S(\omega(t)) = \begin{bmatrix} 0 & -\omega_\psi(t) & \omega_\theta(t) \\ \omega_\psi(t) & 0 & -\omega_\phi(t) \\ -\omega_\theta(t) & \omega_\phi(t) & 0 \end{bmatrix} \quad (2.11)$$

The time derivative of the rotation matrix, (2.10), gives an implicit relationship between the Euler angles measured by the compass and the angular rates measured by the gyros. Making this relationship explicit by taking the time-derivative of (2.6) and solving for the angular rates will achieve the goal of deriving a system model that relates gyro data to compass data.

Alternately, (2.10) may also be expressed with respect to (2.7), (2.8), and (2.9) as

$$\begin{aligned}\dot{R}_x(\phi(t)) &= \frac{dR}{d\phi} \frac{d\phi}{dt} = \dot{\phi} S(i) R_x(\phi(t)) \\ \dot{R}_y(\theta(t)) &= \frac{dR}{d\theta} \frac{d\theta}{dt} = \dot{\theta} S(j) R_y(\theta(t)) \\ \dot{R}_z(\psi(t)) &= \frac{dR}{d\psi} \frac{d\psi}{dt} = \dot{\psi} S(k) R_z(\psi(t)),\end{aligned}\tag{2.12}$$

where

$$i = \begin{bmatrix} 1 \\ 0 \\ 0 \end{bmatrix}, \quad j = \begin{bmatrix} 0 \\ 1 \\ 0 \end{bmatrix}, \quad \text{and} \quad k = \begin{bmatrix} 0 \\ 0 \\ 1 \end{bmatrix}\tag{2.13}$$

are unit vectors pointing in the x, y, z directions, respectively. Furthermore, two other properties are useful.

$$R(\eta(t)) R^T(\eta(t)) = R^T(\eta(t)) R(\eta(t)) = I \quad \text{and}\tag{2.14}$$

$$R(\eta(t)) S(\omega(t)) R^T(\eta(t)) = S(R(\eta(t)) \omega(t)).\tag{2.15}$$

The time derivative, $\dot{R}_B^N(\eta(t))$, of (2.6) can now be easily calculated using the relationships, (2.12), (2.14), and (2.15). Note that time dependence notation is suppressed for simplicity.

$$\begin{aligned}\dot{R}_B^N(\eta) &= \frac{d}{d\phi} (R_x(\phi)) R_y(\theta) R_z(\psi) \dot{\phi} + R_x(\phi) \frac{d}{d\theta} (R_y(\theta)) R_z(\psi) \dot{\theta} + R_x(\phi) R_y(\theta) \frac{d}{d\psi} (R_z(\psi)) \dot{\psi} \\ &= S(i) R_x(\phi) R_y(\theta) R_z(\psi) \dot{\phi} + R_x(\phi) S(j) R_y(\theta) R_z(\psi) \dot{\theta} + R_x(\phi) R_y(\theta) S(k) R_z(\psi) \dot{\psi} \\ &= S(i) R_x(\phi) R_y(\theta) R_z(\psi) \dot{\phi} + (R_x(\phi) S(j) R_x^T(\phi)) R_x(\phi) R_y(\theta) R_z(\psi) \dot{\theta} \\ &\quad + (R_x(\phi) (R_y(\theta) S(k) R_y^T(\theta)) R_x^T(\phi)) R_x(\phi) R_y(\theta) R_z(\psi) \dot{\psi} \\ &= S(i) R_B^N(\eta) \dot{\phi} + S(R_x(\phi) j) R_B^N(\eta) \dot{\theta} + S(R_x(\phi) R_y(\theta) k) R_B^N(\eta) \dot{\psi}\end{aligned}\tag{2.16}$$

Setting this expression equal to the right-hand side of (2.10) and taking advantage of the linearity of a skew symmetric matrix function yields

$$S(\omega(t)) = S(i\dot{\phi} + R_x(\phi)j\dot{\theta} + R_x(\phi)R_y(\theta)k\dot{\psi}),\tag{2.17}$$

which is simplified by taking the vector equivalent of the skew-symmetric matrices.

$$\begin{bmatrix} \omega_\phi(t) \\ \omega_\theta(t) \\ \omega_\psi(t) \end{bmatrix} = \begin{bmatrix} \dot{\phi}(t) \\ 0 \\ 0 \end{bmatrix} + R_x(\phi) \begin{bmatrix} 0 \\ \dot{\theta}(t) \\ 0 \end{bmatrix} + R_x(\phi)R_y(\theta) \begin{bmatrix} 0 \\ 0 \\ \dot{\psi}(t) \end{bmatrix} \quad (2.18)$$

Expressing (2.18) in matrix notation gives an explicit expression for body-fixed angular rates in terms of Euler angular rates.

$$\begin{bmatrix} \omega_\phi(t) \\ \omega_\theta(t) \\ \omega_\psi(t) \end{bmatrix} = \begin{bmatrix} 1 & 0 & -\sin \theta(t) \\ 0 & \cos \phi(t) & \cos \theta(t) \sin \phi(t) \\ 0 & -\sin \phi(t) & \cos \theta(t) \cos \phi(t) \end{bmatrix} \begin{bmatrix} \dot{\phi}(t) \\ \dot{\theta}(t) \\ \dot{\psi}(t) \end{bmatrix} \quad (2.19)$$

Inverting the coefficient matrix in (2.19) yields the desired mapping. The inversion is defined only when $\theta(t) \neq \pm n\pi/2$ for $n = 1, 2, 3, \dots$, which corresponds to the vehicle's nose not pointing straight up or down.

$$\begin{bmatrix} \dot{\phi}(t) \\ \dot{\theta}(t) \\ \dot{\psi}(t) \end{bmatrix} = \begin{bmatrix} 1 & \sin \phi(t) \tan \theta(t) & \cos \phi(t) \tan \theta(t) \\ 0 & \cos \phi(t) & -\sin \phi(t) \\ 0 & \frac{\sin \phi(t)}{\cos \theta(t)} & \frac{\cos \phi(t)}{\cos \theta(t)} \end{bmatrix} \begin{bmatrix} \omega_\phi(t) \\ \omega_\theta(t) \\ \omega_\psi(t) \end{bmatrix} \quad (2.20)$$

Correcting for scale and bias errors in (2.20) with (2.3) accurately relates measured gyroscope rates to the Euler rates.

$$\begin{bmatrix} \dot{\phi}(t) \\ \dot{\theta}(t) \\ \dot{\psi}(t) \end{bmatrix} = \begin{bmatrix} 1 & \sin \phi(t) \tan \theta(t) & \cos \phi(t) \tan \theta(t) \\ 0 & \cos \phi(t) & -\sin \phi(t) \\ 0 & \frac{\sin \phi(t)}{\cos \theta(t)} & \frac{\cos \phi(t)}{\cos \theta(t)} \end{bmatrix} \begin{pmatrix} \begin{bmatrix} \bar{a}_\phi & 0 & 0 \\ 0 & \bar{a}_\theta & 0 \\ 0 & 0 & \bar{a}_\psi \end{bmatrix} \begin{bmatrix} \omega_{\phi,m}(t) \\ \omega_{\theta,m}(t) \\ \omega_{\psi,m}(t) \end{bmatrix} + \begin{bmatrix} \bar{b}_\phi \\ \bar{b}_\theta \\ \bar{b}_\psi \end{bmatrix} \end{pmatrix} \quad (2.21)$$

$$y(t) = \begin{bmatrix} 1 & 0 & 0 \\ 0 & 1 & 0 \\ 0 & 0 & 1 \end{bmatrix} \begin{bmatrix} \phi(t) \\ \theta(t) \\ \psi(t) \end{bmatrix}$$

Throughout the remainder of this paper, (2.21) will be referred to as the system or plant model.

Chapter 3

Gyroscope Calibration

When designing autonomous vehicles, it is desirable to minimize the amount of user interaction. Calibration routines vary from look-up tables, [3], to real-time parameter identification, [12]. The method chosen for a particular application will depend on the onboard processing power available as well as the ease with which the system can be modeled. A look-up table is an ideal solution for sensors that have predictable performance. Sensors with time-varying errors are difficult to model and tend to require a more flexible calibration routine, which will require more processing power.

3.1 Motivation

As mentioned in Chapter 2, the unknown parameters present in gyro performance vary based on a number of factors that are difficult to model. Therefore, a real time parameter identification algorithm is desirable. With the goal of autonomous operation, an adaptive approach will be examined.

Typically, when a system has a set of unknown parameters, a Kalman filter is applied to the system after it has been augmented with unknown parameter states. This approach was examined as a possible solution to the gyro parameter estimation problem. When the parameters of the gyro are augmented in the state, the system is *locally* unobservable. A Kalman filter requires that the system be locally observable to estimate the unknown parameters accurately. Therefore, this approach could not be implemented. This section presents the observability analysis of the system and shows why the system fails to be observable.

A linear system,

$$\begin{aligned} \dot{x}(t) &= A(t)x(t), & x(t_0) &= x_0 \\ y(t) &= C(t)x(t) \end{aligned} \tag{3.1}$$

is called *observable* on a finite interval, $[t_0, t_f]$ if the initial state, $x(t_0) = x_0$, is uniquely determined by the corresponding output $y(t)$ for $t \in [t_0, t_f]$, [10]. That is, by using the system output and the known system model, the initial state can be determined.

To test observability on the gyro model, (2.21), unknown states are first augmented into the

system to generate a state vector, $z(t) \in \mathbb{R}^{9 \times 1}$.

$$\begin{aligned}
 \begin{bmatrix} \dot{\phi} \\ \dot{\bar{a}}_\phi \\ \dot{\bar{b}}_\phi \\ \dot{\theta} \\ \dot{\bar{a}}_\theta \\ \dot{\bar{b}}_\theta \\ \dot{\psi} \\ \dot{\bar{a}}_\psi \\ \dot{\bar{b}}_\psi \end{bmatrix} &= \begin{bmatrix} (\bar{a}_\phi \omega_\phi + \bar{b}_\phi) + \sin \phi \tan \theta (\bar{a}_\theta \omega_\theta + \bar{b}_\theta) + \cos \phi \tan \theta (\bar{a}_\psi \omega_\psi + \bar{b}_\psi) \\ 0 \\ 0 \\ \cos(\phi) (\bar{a}_\theta \omega_\theta + \bar{b}_\theta) - \sin \phi (\bar{a}_\psi \omega_\psi + \bar{b}_\psi) \\ 0 \\ 0 \\ \frac{\sin \phi}{\cos \theta} (\bar{a}_\theta \omega_\theta + \bar{b}_\theta) + \frac{\cos \phi}{\cos \theta} (\bar{a}_\psi \omega_\psi + \bar{b}_\psi) \\ 0 \\ 0 \end{bmatrix} \\
 y(t) &= \begin{bmatrix} 1 & 0 & 0 & 0 & 0 & 0 & 0 & 0 & 0 \\ 0 & 0 & 0 & 1 & 0 & 0 & 0 & 0 & 0 \\ 0 & 0 & 0 & 0 & 0 & 0 & 1 & 0 & 0 \end{bmatrix}
 \end{aligned} \tag{3.2}$$

The system (3.2) is linearized about an arbitrary trajectory by taking the Jacobian of state and measurement equations

$$\begin{aligned}
 \bar{A}(t) &= \frac{\partial}{\partial z} f(\bar{z}(t), \bar{u}(t), t) \\
 \bar{B}(t) &= \frac{\partial}{\partial u} f(\bar{z}(t), \bar{u}(t), t) \\
 \bar{C}(t) &= \frac{\partial}{\partial z} h(\bar{z}(t), \bar{u}(t), t)
 \end{aligned} \tag{3.3}$$

where $\bar{z}(t)$ and $\bar{u}(t)$ represent the nominal trajectory. Note that this system already has a linear C matrix. The resulting system is

$$\begin{aligned}
 \dot{z}_\delta(t) &= \bar{A}(t)z_\delta(t) + \bar{B}(t)u_\delta(t), \quad z_\delta(0) = z_{\delta 0} \\
 y_\delta(t) &= \bar{C}(t)z_\delta(t)
 \end{aligned} \tag{3.4}$$

where $\bar{A}(t) \in R^{9 \times 9}$, $\bar{B}(t) \in R^{9 \times 3}$, and $\bar{C}(t) \in R^{3 \times 9}$ for $t \in [t_0, t_f]$. Observability is verified by testing for invertibility of the observability Gramian,

$$M(t_0, t_f) = \int_{t_0}^{t_f} \Phi^T(\sigma, t_0) \bar{C}^T(\sigma) \bar{C}(\sigma) \Phi(\sigma, t_0) d\sigma \tag{3.5}$$

where $\Phi^T(t, t_0)$ is the transition matrix of the linearized system. Due to the complexity of this system, solving for the transition matrix directly is particularly difficult. Therefore, (3.5) is rewritten in differential form,

$$\dot{M}(t, t_f) = -A^T(t)M(t, t_f) - M(t, t_f)A(t) - C^T(t)C(t), \quad M(t_0, t_f) = 0. \quad (3.6)$$

The solution of (3.6) is computed numerically. Using numerical data collected during three different vehicle actions: diving, steady-state straight-line trajectories, and turning, specific instances of system stability can be examined.

Diving: $[\phi, \theta, \psi, \omega_\phi, \omega_\theta, \omega_\psi] = [15, -15, 90, 12, 10, 5]$

Straight-Line: $[\phi, \theta, \psi, \omega_\phi, \omega_\theta, \omega_\psi] = [5, 5, 90, 4, 4, 4]$

Turning: $[\phi, \theta, \psi, \omega_\phi, \omega_\theta, \omega_\psi] = [10, 5, 45, 10, 5, 15]$

In each case, the yaw angle is arbitrary, as it does not appear in the system model. Gyroscope error parameters are set to nominal values ($\bar{a}_\eta = 1, \bar{b}_\eta = 0$) because the system must be observable when the error is assumed not to exist. In all cases, the $rank(M) = 6 < 9$ which means that the Gramian is not invertible. Therefore, the system cannot be observable for any $t \in [t_0, t_f]$. While observability may exist for some set of input and state values, conditional observability of a system under normal operating conditions is not acceptable. Therefore, a Kalman filter approach to the system identification is not feasible.

Another method must therefore be utilized to solve for the unknown parameters. By applying an adaptive identifier algorithm, the nonlinear system can be used entirely to estimate true parameter values. The goal of an adaptive identifier algorithm is to identify all unknown system parameters by comparing estimated state values to a reference signal and recursively adjusting the parameters to bring the error between estimated and reference (true) signals to zero. At the same time, the algorithm keeps all signals bounded. Parameter values

will be shown to converge under sufficient persistence of excitation. Applied to the gyro system, excitation means that each axis senses sufficient angular rates over time such that the identifier is able to converge upon the correct identifier values. When this condition is not met, the parameters may converge to an incorrect value.

3.2 Adaptive Parameter Identification

We consider the class of systems with the state structure,

$$\dot{x}(t) = f^T(t)\beta \quad (3.7)$$

where $f^T(t)$ describes the system's dynamics and β is a lumped vector of unknown parameters. The output of the system is compared to a reference signal or system. The resulting error signal forms the input to a set of parameter and state estimation update laws, which adjust the system parameter values based on the magnitude of the error signal.

The gyro model is first rewritten in the desired system state structure before applying the adaptive identifier. The following vectors are defined

$$f_\phi(t) = \begin{bmatrix} \omega_{\phi,m}(t) \\ 1 \end{bmatrix}, f_\theta(t) = \begin{bmatrix} \omega_{\theta,m}(t) \\ 1 \end{bmatrix}, f_\psi(t) = \begin{bmatrix} \omega_{\psi,m}(t) \\ 1 \end{bmatrix} \quad (3.8)$$

and

$$\beta_\phi = \begin{bmatrix} \bar{a}_\phi \\ \bar{b}_\phi \end{bmatrix}, \beta_\theta = \begin{bmatrix} \bar{a}_\theta \\ \bar{b}_\theta \end{bmatrix}, \beta_\psi = \begin{bmatrix} \bar{a}_\psi \\ \bar{b}_\psi \end{bmatrix}. \quad (3.9)$$

It will become useful to combine (3.9) into one vector

$$\beta_\eta = \begin{bmatrix} \beta_\phi \\ \beta_\theta \\ \beta_\psi \end{bmatrix} \quad (3.10)$$

The vectors, (3.8) and (3.9), allow for the following substitution from (2.3),

$$\begin{bmatrix} \bar{a}_\phi & 0 & 0 \\ 0 & \bar{a}_\theta & 0 \\ 0 & 0 & \bar{a}_\psi \end{bmatrix} \begin{bmatrix} \omega_{\phi,m}(t) \\ \omega_{\theta,m}(t) \\ \omega_{\psi,m}(t) \end{bmatrix} + \begin{bmatrix} \bar{b}_\phi \\ \bar{b}_\theta \\ \bar{b}_\psi \end{bmatrix} = \begin{bmatrix} f_\phi^T(t)\beta_\phi \\ f_\theta^T(t)\beta_\theta \\ f_\psi^T(t)\beta_\psi \end{bmatrix} \quad (3.11)$$

which is then substituted into (2.21).

$$\begin{bmatrix} \dot{\phi}(t) \\ \dot{\theta}(t) \\ \dot{\psi}(t) \end{bmatrix} = \begin{bmatrix} 1 & \sin \phi(t) \tan \theta(t) & \cos \phi(t) \tan \theta(t) \\ 0 & \cos \phi(t) & -\sin \phi(t) \\ 0 & \frac{\sin \phi(t)}{\cos \theta(t)} & \frac{\cos \phi(t)}{\cos \theta(t)} \end{bmatrix} \begin{bmatrix} f_\phi^T(t)\beta_\phi \\ f_\theta^T(t)\beta_\theta \\ f_\psi^T(t)\beta_\psi \end{bmatrix} \quad (3.12)$$

The trigonometric elements of the matrix of coefficients in (3.12) are replaced with the terms, γ_i to allow for better readability.

$$\begin{aligned} \gamma_1(\phi(t), \theta(t)) &= \sin \phi(t) \tan \theta(t) \\ \gamma_2(\phi(t), \theta(t)) &= \cos \phi(t) \tan \theta(t) \\ \gamma_3(\phi(t)) &= \cos \phi(t) \\ \gamma_4(\phi(t)) &= -\sin \phi(t) \\ \gamma_5(\phi(t), \theta(t)) &= \frac{\sin \phi(t)}{\cos \theta(t)} \\ \gamma_6(\phi(t), \theta(t)) &= \frac{\cos \phi(t)}{\cos \theta(t)} \end{aligned}$$

Finally, the vectors $f_\phi^T(t)$, $f_\theta^T(t)$, $f_\psi^T(t)$ are moved into the coefficient matrix to isolate the unknown parameters.

$$\begin{bmatrix} \dot{\phi}(t) \\ \dot{\theta}(t) \\ \dot{\psi}(t) \end{bmatrix} = \begin{bmatrix} f_\phi^T(t) & \gamma_1(\phi(t), \theta(t))f_\theta^T(t) & \gamma_2(\phi(t), \theta(t))f_\psi^T(t) \\ 0 & \gamma_3(\phi(t))f_\theta^T(t) & \gamma_4(\phi(t))f_\psi^T(t) \\ 0 & \gamma_5(\phi(t), \theta(t))f_\theta^T(t) & \gamma_6(\phi(t), \theta(t))f_\psi^T(t) \end{bmatrix} \begin{bmatrix} \beta_\phi \\ \beta_\theta \\ \beta_\psi \end{bmatrix} \quad (3.13)$$

The gyroscope model is now in the form, $\dot{\eta} = F^T(t)\beta_\eta$ where $F^T(t)$ is the system dynamics, and β_η is the vector of unknown parameters.

3.2.1 Defining Parameter Update Functions

Upon the system structure, (3.7), the identifier is designed. Error equations for the state and parameters are defined as

$$\tilde{\eta}(t) = \eta(t) - \hat{\eta}(t) \quad (3.14)$$

$$\dot{\tilde{\eta}}(t) = \dot{\eta}(t) - \dot{\hat{\eta}}(t) \quad (3.15)$$

$$\tilde{\beta}_\eta(t) = \beta_\eta - \hat{\beta}_\eta(t) \quad (3.16)$$

$$\dot{\tilde{\beta}}_\eta(t) = -\dot{\hat{\beta}}_\eta(t). \quad (3.17)$$

where

$$\eta(t) = \begin{bmatrix} \phi(t) & \theta(t) & \psi(t) \end{bmatrix}^T \text{ and } \beta_\eta = \begin{bmatrix} \beta_\phi & \beta_\theta & \beta_\psi \end{bmatrix}^T \quad (3.18)$$

are the previously defined measurements,

$$\hat{\eta}(t) = \begin{bmatrix} \hat{\phi}(t) & \hat{\theta}(t) & \hat{\psi}(t) \end{bmatrix}^T \text{ and } \hat{\beta}_\eta(t) = \begin{bmatrix} \hat{\beta}_\phi(t) & \hat{\beta}_\theta(t) & \hat{\beta}_\psi(t) \end{bmatrix}^T \quad (3.19)$$

are corresponding estimates, and

$$\tilde{\eta}(t) = \begin{bmatrix} \tilde{\phi}(t) & \tilde{\theta}(t) & \tilde{\psi}(t) \end{bmatrix}^T \text{ and } \tilde{\beta}_\eta(t) = \begin{bmatrix} \tilde{\beta}_\phi(t) & \tilde{\beta}_\theta(t) & \tilde{\beta}_\psi(t) \end{bmatrix}^T \quad (3.20)$$

are the errors between measurements and estimates. Note that $\dot{\beta}_\eta = 0$ since the true parameter error is a constant. Based on these error equations, a Lyapunov function candidate is defined as

$$\begin{aligned} V(\tilde{\eta}, \tilde{\beta}_\eta) &= \frac{1}{2} \tilde{\eta}^T(t) \tilde{\eta}(t) + \frac{1}{2} \tilde{\beta}_\eta^T(t) \Lambda^{-1} \tilde{\beta}_\eta(t) \\ &= \frac{1}{2} \tilde{\phi}^T(t) \tilde{\phi}(t) + \frac{1}{2} \tilde{\theta}^T(t) \tilde{\theta}(t) + \frac{1}{2} \tilde{\psi}^T(t) \tilde{\psi}(t) \\ &\quad + \frac{1}{2} \tilde{\beta}_\phi^T(t) \Lambda_\phi^{-1} \tilde{\beta}_\phi(t) + \frac{1}{2} \tilde{\beta}_\theta^T(t) \Lambda_\theta^{-1} \tilde{\beta}_\theta(t) \\ &\quad + \frac{1}{2} \tilde{\beta}_\psi^T(t) \Lambda_\psi^{-1} \tilde{\beta}_\psi(t). \end{aligned} \quad (3.21)$$

such that $V(\tilde{\eta}, \tilde{\beta}_\eta) > 0$ and $\Lambda \in \mathbb{R}^{6 \times 6}$ is a tuning matrix

$$\Lambda = \begin{bmatrix} \Lambda_\phi & 0 & 0 \\ 0 & \Lambda_\theta & 0 \\ 0 & 0 & \Lambda_\psi \end{bmatrix} \quad (3.22)$$

with

$$\Lambda_\phi = \begin{bmatrix} \lambda_1 & 0 \\ 0 & \lambda_2 \end{bmatrix} \quad \Lambda_\theta = \begin{bmatrix} \lambda_3 & 0 \\ 0 & \lambda_4 \end{bmatrix} \quad \Lambda_\psi = \begin{bmatrix} \lambda_5 & 0 \\ 0 & \lambda_6 \end{bmatrix} \quad (3.23)$$

for $\lambda_i > 0$. The corresponding time derivative is

$$\begin{aligned} \dot{V}(\tilde{\eta}, \tilde{\beta}_\eta) &= \tilde{\phi}^T(t)\dot{\tilde{\phi}}(t) + \tilde{\theta}^T(t)\dot{\tilde{\theta}}(t) + \tilde{\psi}^T(t)\dot{\tilde{\psi}}(t) \\ &\quad - \tilde{\beta}_\phi^T(t)\Lambda_\phi^{-1}\dot{\tilde{\beta}}_\phi(t) - \tilde{\beta}_\theta^T(t)\Lambda_\theta^{-1}\dot{\tilde{\beta}}_\theta(t) \\ &\quad - \tilde{\beta}_\psi^T(t)\Lambda_\psi^{-1}\dot{\tilde{\beta}}_\psi(t) \end{aligned} \quad (3.24)$$

where the relationship from (3.17) has been used. We choose update laws

$$\dot{\hat{\eta}}(t) = -K_\eta\tilde{\eta}(t) + F^T(t)\hat{\beta}_\eta(t) \quad \text{and} \quad (3.25)$$

$$\dot{\hat{\beta}}_\eta(t) = \Lambda F(t)\tilde{\eta}(t) \quad (3.26)$$

such that \dot{V} becomes negative semi-definite. The matrix

$$K_\eta = \begin{bmatrix} K_\phi & 0 & 0 \\ 0 & K_\theta & 0 \\ 0 & 0 & K_\psi \end{bmatrix} \quad (3.27)$$

represents the scalar gains for each axis to control the rate of update. Equations (3.14) and (3.15) are used to rewrite (3.25) in terms of $\dot{\hat{\eta}}(t)$.

$$\begin{aligned} \dot{\hat{\eta}}(t) &= \dot{\eta}(t) - \dot{\hat{\eta}}(t) \\ &= F^T(t)\beta_\eta + K_\eta\tilde{\eta}(t) - F^T(t)\hat{\beta}_\eta(t) \\ &= K_\eta\tilde{\eta}(t) + F^T(t)\tilde{\beta}_\eta(t) \end{aligned} \quad (3.28)$$

Writing (3.26) and (3.28) explicitly in terms of each axis gives the six update equations.

$$\begin{aligned} \dot{\tilde{\phi}}(t) &= K_\phi\tilde{\phi}(t) + f_\phi^T(t)\tilde{\beta}_\phi(t) \\ &\quad + \gamma_1(\phi(t), \theta(t))f_\theta^T(t)\tilde{\beta}_\theta(t) \\ &\quad + \gamma_2(\phi(t), \theta(t))f_\psi^T(t)\tilde{\beta}_\psi(t) \end{aligned} \quad (3.29)$$

$$\begin{aligned}
\dot{\tilde{\theta}}(t) &= K_{\theta}\tilde{\theta}(t) \\
&+ \gamma_3(\phi(t))f_{\theta}^T(t)\tilde{\beta}_{\theta}(t) \\
&+ \gamma_4(\phi(t))f_{\psi}^T(t)\tilde{\beta}_{\psi}(t)
\end{aligned} \tag{3.30}$$

$$\begin{aligned}
\dot{\tilde{\psi}}(t) &= K_{\psi}\tilde{\psi}(t) \\
&+ \gamma_5(\phi(t), \theta(t))f_{\theta}^T(t)\tilde{\beta}_{\theta}(t) \\
&+ \gamma_6(\phi(t), \theta(t))f_{\psi}^T(t)\tilde{\beta}_{\psi}(t)
\end{aligned} \tag{3.31}$$

and

$$\dot{\hat{\beta}}_{\phi}(t) = \Lambda_{\phi}f_{\phi}(t)\tilde{\phi}(t) \tag{3.32}$$

$$\begin{aligned}
\dot{\hat{\beta}}_{\theta}(t) &= \gamma_1(\phi(t), \theta(t))\Lambda_{\theta}f_{\theta}(t)\tilde{\phi}(t) \\
&+ \gamma_3(\phi(t))\Lambda_{\theta}f_{\theta}(t)\tilde{\theta}(t) \\
&+ \gamma_5(\phi(t), \theta(t))\Lambda_{\theta}f_{\theta}(t)\tilde{\psi}(t)
\end{aligned} \tag{3.33}$$

$$\begin{aligned}
\dot{\hat{\beta}}_{\psi}(t) &= \gamma_2(\phi(t), \theta(t))\Lambda_{\psi}f_{\psi}(t)\tilde{\phi}(t) \\
&+ \gamma_4(\phi(t))\Lambda_{\psi}f_{\psi}(t)\tilde{\theta}(t) \\
&+ \gamma_6(\phi(t), \theta(t))\Lambda_{\psi}f_{\psi}(t)\tilde{\psi}(t)
\end{aligned} \tag{3.34}$$

3.2.2 Lyapunov Stability Analysis

The negative semi-definiteness of the Lyapunov candidate can now be verified using the update laws. Note that time dependence notation is suppressed for simplicity.

$$\begin{aligned}
\dot{V}(\tilde{\eta}, \tilde{\beta}_\eta) &= \tilde{\phi}^T K_\phi \tilde{\phi} + \tilde{\theta}^T K_\theta \tilde{\theta} + \tilde{\psi}^T K_\psi \tilde{\psi} \\
&\quad + \tilde{\phi}^T f_\phi^T \tilde{\beta}_\phi + \gamma_1 \tilde{\phi}^T f_\theta^T \tilde{\beta}_\theta + \gamma_2 \tilde{\phi}^T f_\psi^T \tilde{\beta}_\psi \\
&\quad + \gamma_3 \tilde{\theta}^T f_\theta^T \tilde{\beta}_\theta + \gamma_4 \tilde{\theta}^T f_\psi^T \tilde{\beta}_\psi + \gamma_5 \tilde{\psi}^T f_\theta^T \tilde{\beta}_\theta \\
&\quad + \gamma_6 \tilde{\psi}^T f_\psi^T \tilde{\beta}_\psi
\end{aligned} \tag{3.35}$$

$$\begin{aligned}
&\quad - \tilde{\beta}_\phi^T f_\phi \tilde{\phi} - \gamma_1 \tilde{\beta}_\theta^T f_\theta \tilde{\phi} - \gamma_2 \tilde{\beta}_\psi^T f_\psi \tilde{\phi} \\
&\quad - \gamma_3 \tilde{\beta}_\theta^T f_\theta \tilde{\theta} - \gamma_4 \tilde{\beta}_\psi^T f_\psi \tilde{\theta} - \gamma_5 \tilde{\beta}_\theta^T f_\theta \tilde{\psi} \\
&\quad - \gamma_6 \tilde{\beta}_\psi^T f_\psi \tilde{\psi} \\
&= \tilde{\phi}^T(t) K_\phi \tilde{\phi}(t) + \tilde{\theta}^T(t) K_\theta \tilde{\theta}(t) \\
&\quad + \tilde{\psi}^T(t) K_\psi \tilde{\psi}(t) \\
&= \tilde{\eta}^T(t) K_\eta \tilde{\eta}(t)
\end{aligned} \tag{3.36}$$

The final equation is obtained by observing that the terms in (3.35) are scalars. By requiring that $K_\eta < 0$, it is apparent that $\dot{V}(\tilde{\eta}, \tilde{\beta}_\eta)$ is negative semi-definite. Barbalat's Lemma is used to state the convergence of the state estimation errors.

Lemma 3.2.1 (Barbalat's Lemma) *Let $\phi : \mathbb{R} \rightarrow \mathbb{R}$ be a uniformly continuous function on $[0, \infty)$. Suppose that $\lim_{t \rightarrow \infty} \int_0^t \phi(\tau) d\tau$ exists and is finite. Then,*

$$\phi(t) \rightarrow 0 \text{ as } t \rightarrow \infty$$

To assess boundedness and convergence, we note the following

1. $\tilde{\eta}(t)$ and $\tilde{\beta}_\eta(t)$ are bounded since the time derivative of the Lyapunov function (3.36) is negative semi-definite.

2. By design of the physical AUV, $\eta(t)$ and $\omega(t)$ are bounded. Therefore, since β_η is a constant, $\dot{\eta}(t)$ is also bounded from (3.13).
3. Using points 1) and 2), $\hat{\eta}(t)$ is bounded from (3.14) and $\hat{\beta}_\eta(t)$ is bounded from (3.16).
4. $\dot{\hat{\eta}}(t)$ is bounded since the terms on the right-hand side of (3.25) are bounded.
5. $\dot{\tilde{\eta}}(t)$ is bounded from (3.15) and points 2) and 4).
6. From (3.36), we conclude that $V(\tilde{\eta}, \tilde{\beta}_\eta)$ is bounded and continuous and from points 1) and 5), $\dot{V}(\tilde{\eta}, \tilde{\beta}_\eta) = \dot{\tilde{\eta}}^T(t)K_\eta\tilde{\eta}(t) + \tilde{\eta}^T(t)K_\eta\dot{\tilde{\eta}}(t)$ is bounded. Therefore, $\dot{V}(\tilde{\eta}, \tilde{\beta}_\eta)$ is continuous. Using Barbalat's Lemma we can conclude that $\lim_{t \rightarrow \infty} \dot{V}(\tilde{\eta}, \tilde{\beta}_\eta) = 0$ which implies that $\tilde{\eta}(t) \rightarrow 0$ as $t \rightarrow \infty$, [4].
7. From point 6) and the parameter update law, (3.26), it follows that $\lim_{t \rightarrow \infty} \dot{\tilde{\beta}}_\eta(t) = 0$.

Therefore, all state variables and parameters are bounded. The state identification error, $\tilde{\eta}(t)$, and the derivative of the parameter estimation error, $\dot{\tilde{\beta}}_\eta(t)$ both asymptotically approach zero. Parameter estimation is only shown to be bounded here and it cannot be concluded that the parameter error will asymptotically converge to zero. However, the general system used in this derivation is well known to have parameter convergence in practice, [11], [12], as it will be shown here as well.

3.2.3 Simulation of Adaptive Identifier

To measure the algorithm's performance, test data is generated with a 6 DOF Matlab-based program created by Daniel H. Harris at the University of Maryland. Vehicle dynamics are simulated using hydrodynamic information tailored for a vehicle similar in size to the ASCL AUV. Attitude and angular rates are simulated for 8 different trajectories. The output angular rate data from the simulator is scaled and biased with gyroscope errors before the

adaptive identifier algorithm is applied to estimate these scale and bias errors. The discrete time versions of the state and parameter update equations are used in the algorithm,

$$\hat{\eta}(k) = \hat{\eta}(k-1) + h[-K_\eta \tilde{\eta}(k) + F^T(k) \hat{\beta}_\eta(k)] \quad (3.37)$$

$$\hat{\beta}_\eta(k) = \hat{\beta}_\eta(k-1) + h[\Lambda F(k) \tilde{\eta}(k)] \quad (3.38)$$

where h is the sample period and $k \geq 0$. The initial state estimates are set to the initial angular orientation measurements and the initial parameter estimates are set to $\bar{a}_i = 1$ and $\bar{b}_i = 0$ for $i = \phi, \theta, \psi$. Selecting the elements of K_η and Λ in (3.37) and (3.38) to provide acceptable convergence is mostly a trial and error process, [12]. However, after choosing a few different values and adjusting them based on convergence preferences, it was found that setting the constants to

$$K_\phi = K_\theta = K_\psi = -0.75$$

and

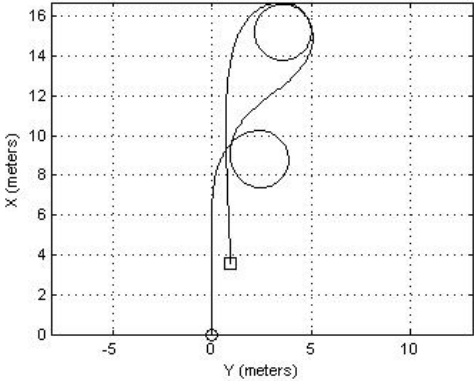
$$\Lambda_\phi = \Lambda_\theta = \Lambda_\psi = \begin{bmatrix} 2 & 0 \\ 0 & 0.2 \end{bmatrix}$$

provides acceptable estimation error. For all simulations, the gyroscope scale and bias factors are set to the values located in Table 3.1. Figure (3.1) contains the vehicle trajectories for

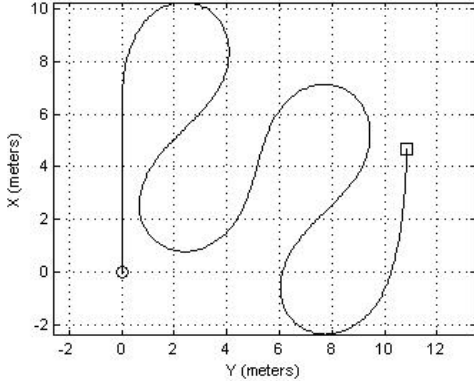
Table 3.1: Simulation settings.

Axis	a	b	\bar{a}	\bar{b}
x	0.1	-0.1	0.9091	0.0909
y	0.1	0.1	0.9091	-0.0909
z	-0.1	0.1	1.1111	-0.1111

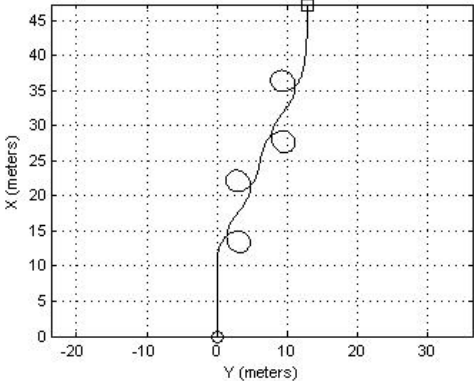
four of the eight simulated paths, while Figures (3.2) through (3.5) show the calibration results from four of the simulated paths. Finally, the parameter convergence is shown for each path in Figures (3.6) through (3.9). In order to obtain a more reasonable simulation, zero mean, Gaussian noise is added to the simulated compass and gyro data.



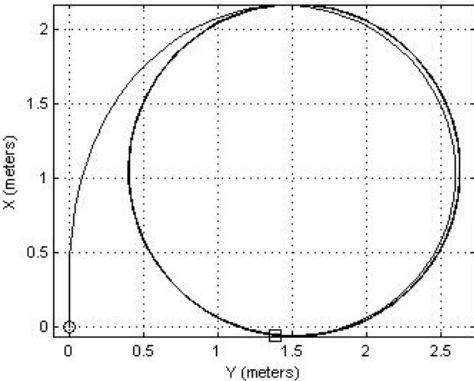
(a) Path 2



(b) Path 3

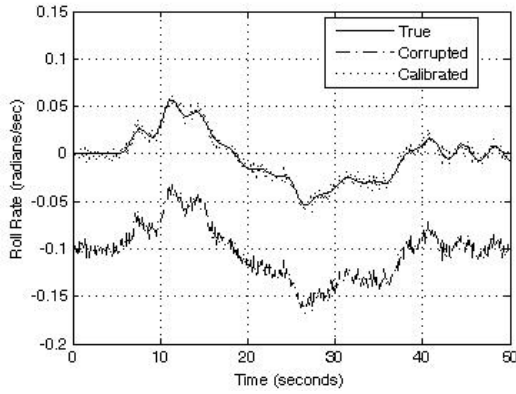


(c) Path 5

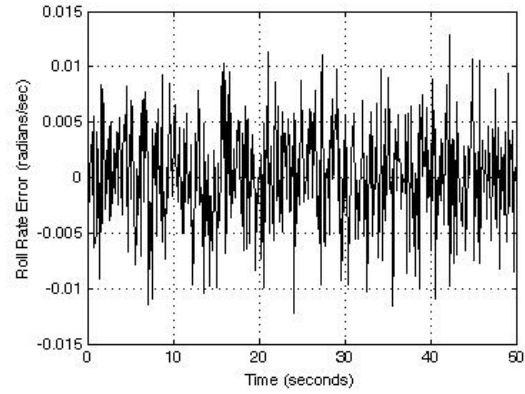


(d) Path 7

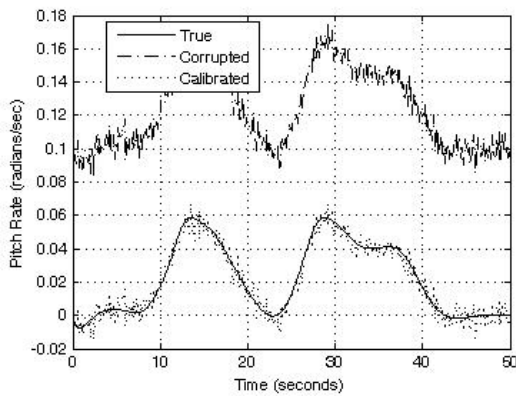
Figure 3.1: Path trajectories for simulation of gyroscope calibration.



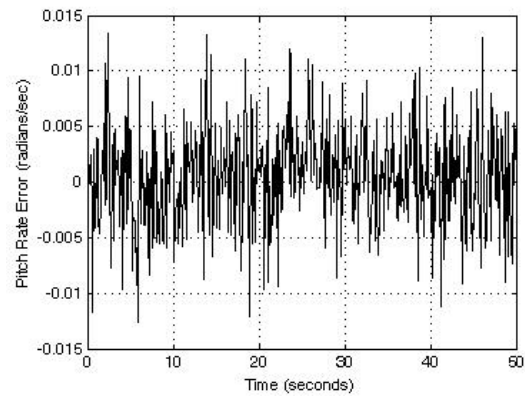
(a) Roll gyroscope response.



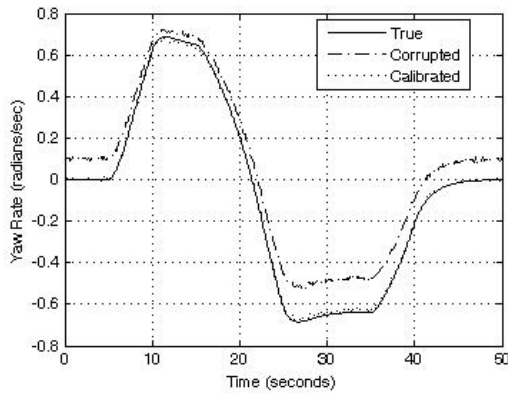
(b) Roll gyroscope response error.



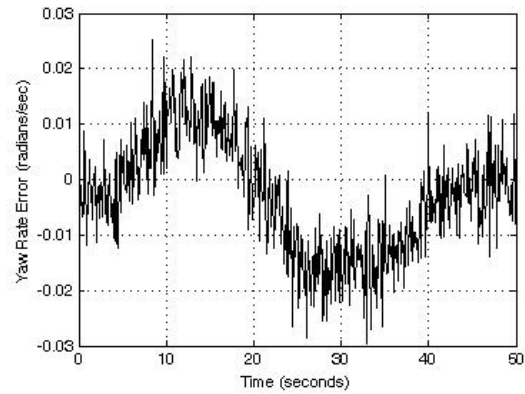
(c) Pitch gyroscope response.



(d) Pitch gyroscope response error.

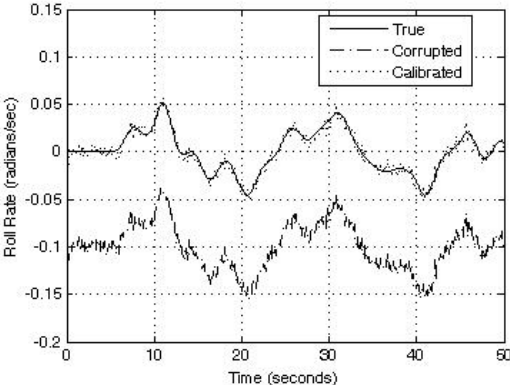


(e) Yaw gyroscope response.

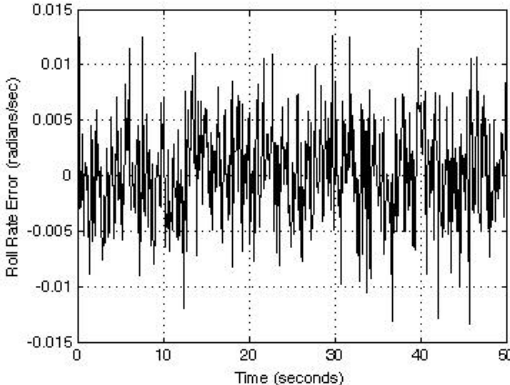


(f) Yaw gyroscope response error.

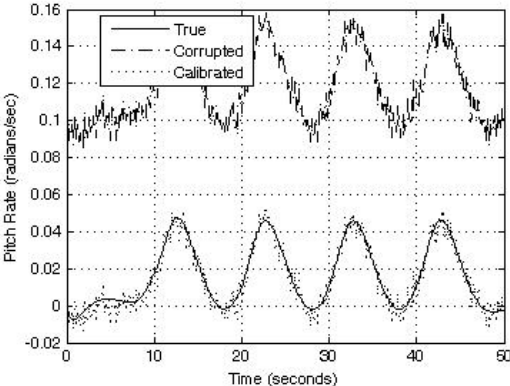
Figure 3.2: Adaptive identifier simulation, path 2.



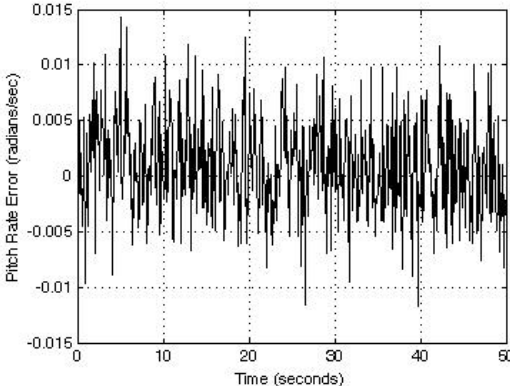
(a) Roll gyroscope response.



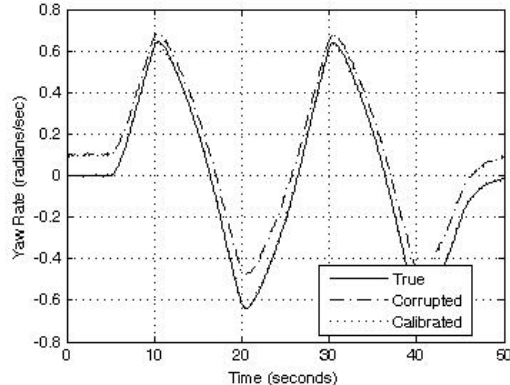
(b) Roll gyroscope response error.



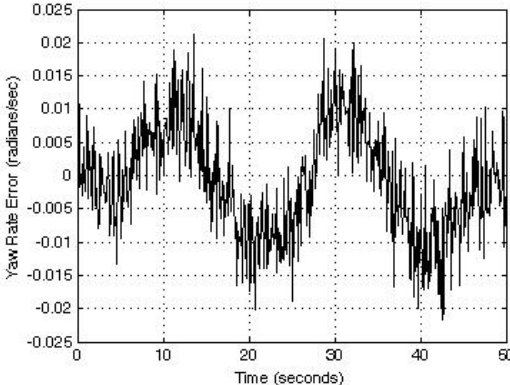
(c) Pitch gyroscope response.



(d) Pitch gyroscope response error.

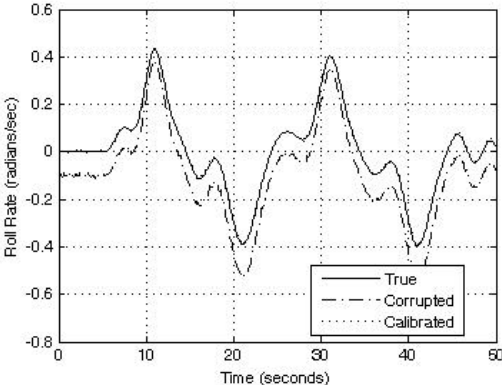


(e) Yaw gyroscope response.

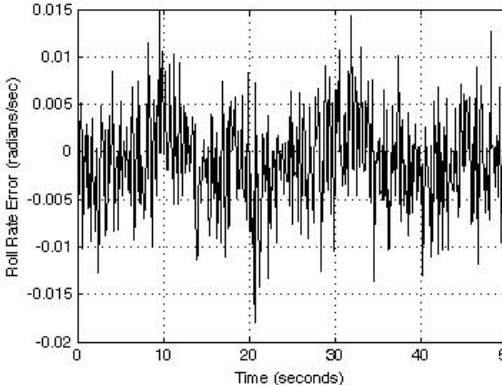


(f) Yaw gyroscope response error.

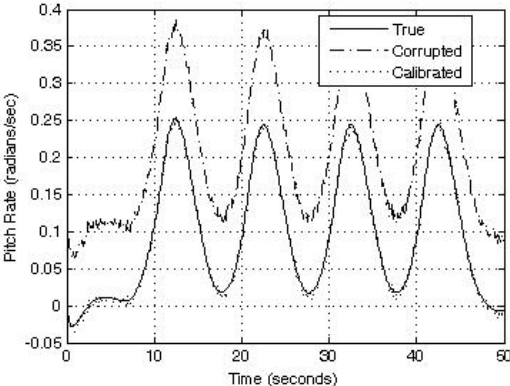
Figure 3.3: Adaptive identifier simulation, path 3.



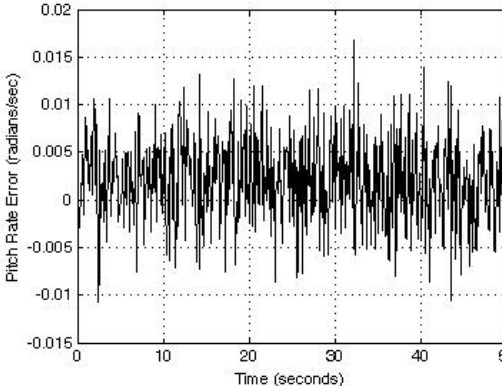
(a) Roll gyroscope response.



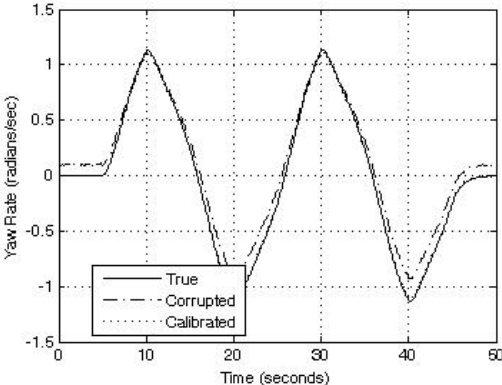
(b) Roll gyroscope response error.



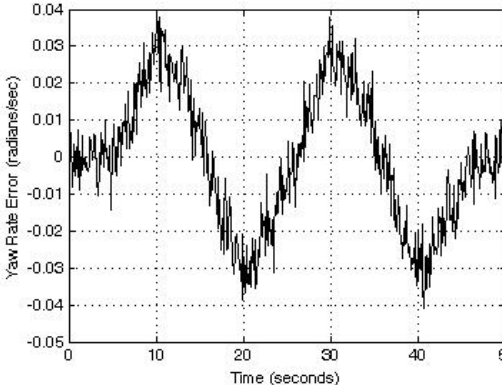
(c) Pitch gyroscope response.



(d) Pitch gyroscope response error.

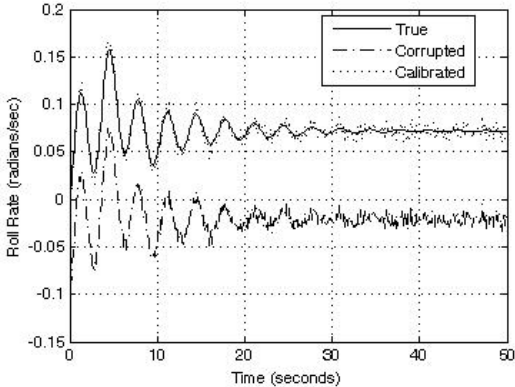


(e) Yaw gyroscope response.

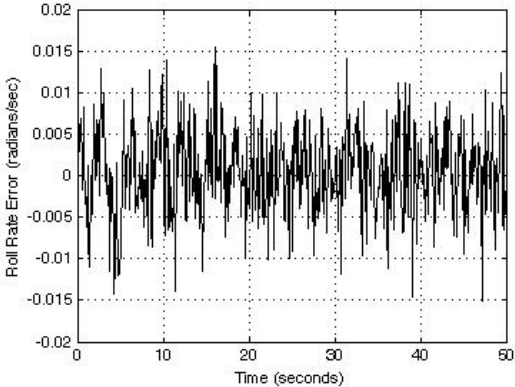


(f) Yaw gyroscope response error.

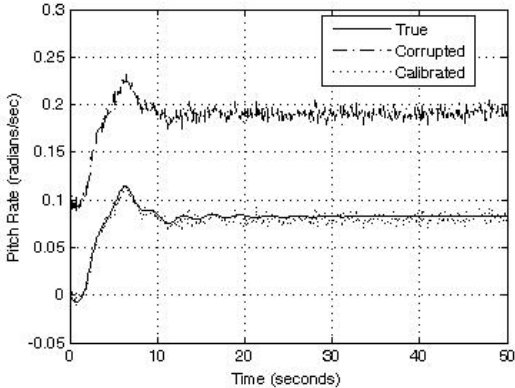
Figure 3.4: Adaptive identifier simulation, path 5.



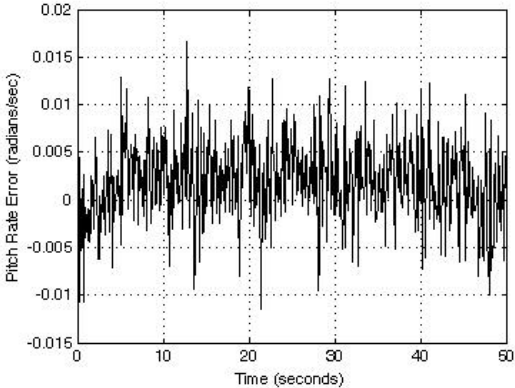
(a) Roll gyroscope response.



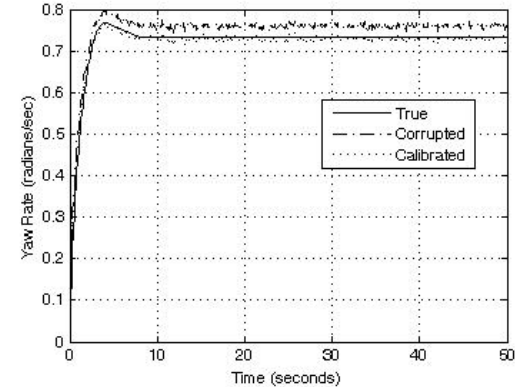
(b) Roll gyroscope response error.



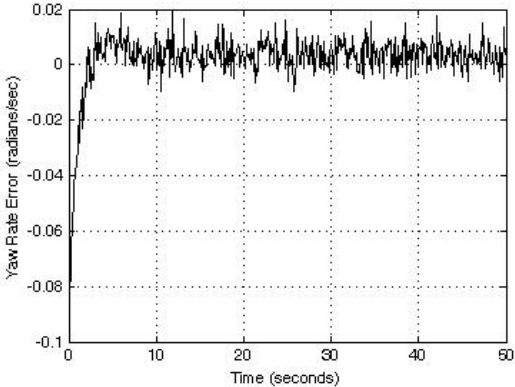
(c) Pitch gyroscope response.



(d) Pitch gyroscope response error.

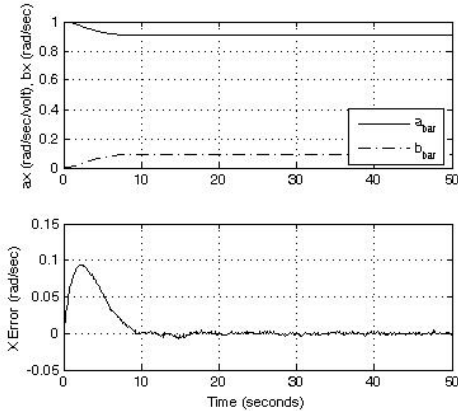


(e) Yaw gyroscope response.

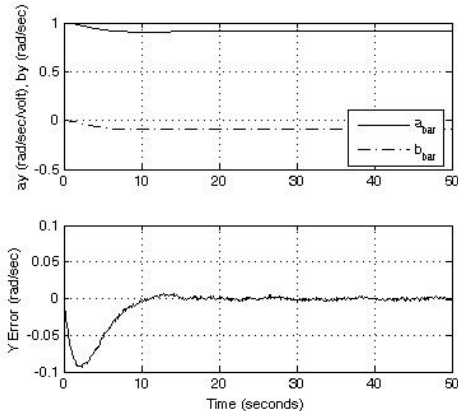


(f) Yaw gyroscope response error.

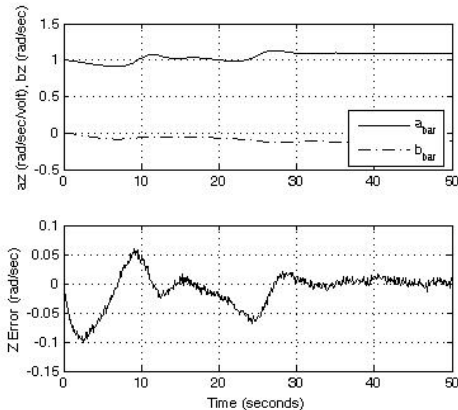
Figure 3.5: Adaptive identifier simulation, path 7.



(a) Roll parameter convergence, path 2.

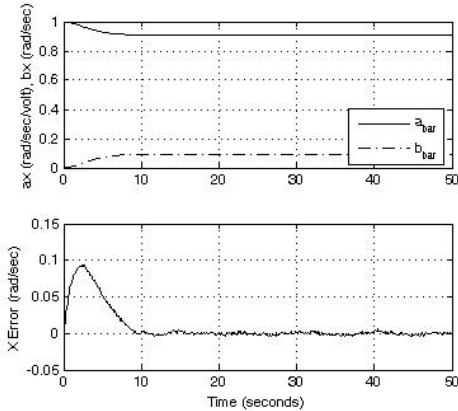


(b) Pitch parameter convergence, path 2.

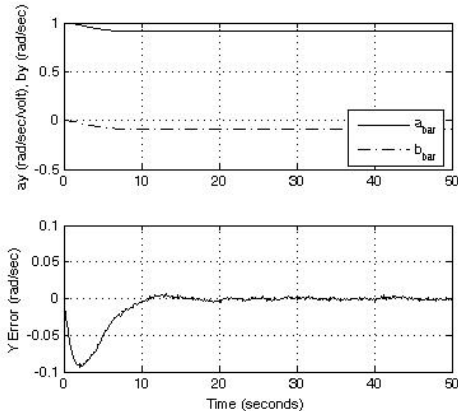


(c) Yaw parameter convergence, path 2.

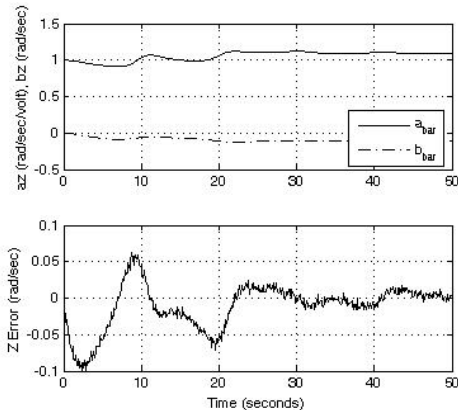
Figure 3.6: Adaptive identifier simulation, path 2 convergence.



(d) Roll parameter convergence, path 3.

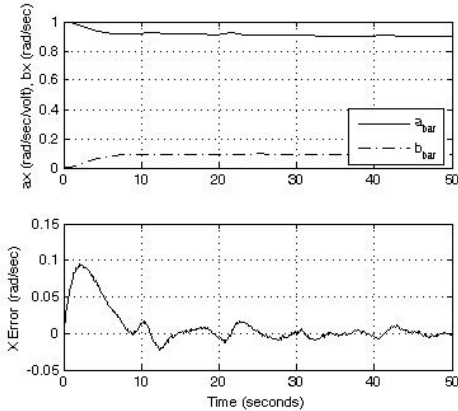


(e) Pitch parameter convergence, path 3.

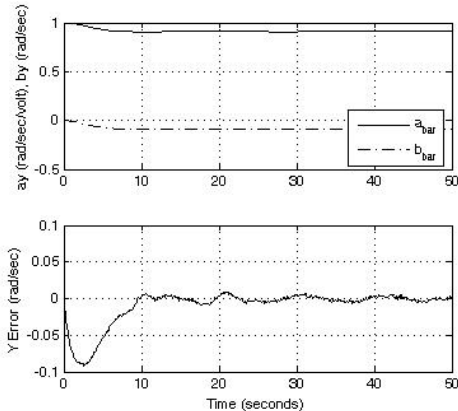


(f) Yaw parameter convergence, path 3.

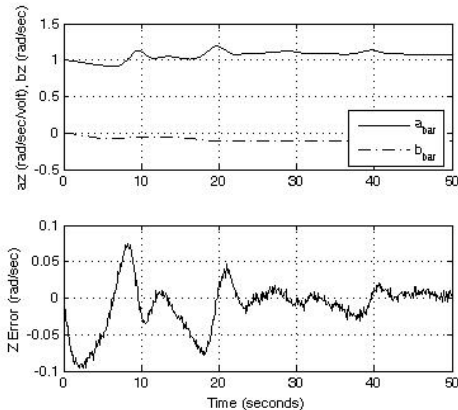
Figure 3.7: Adaptive identifier simulation, path 3 convergence.



(a) Roll parameter convergence, path 5.

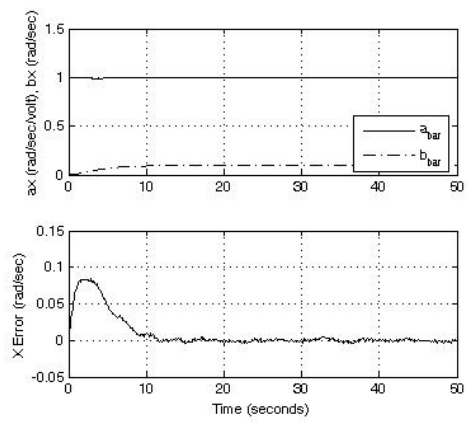


(b) Pitch parameter convergence, path 5.

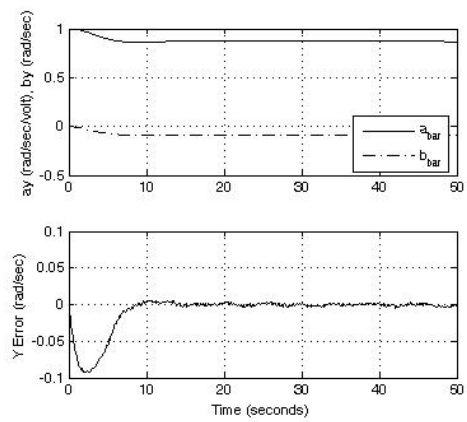


(c) Yaw parameter convergence, path 5.

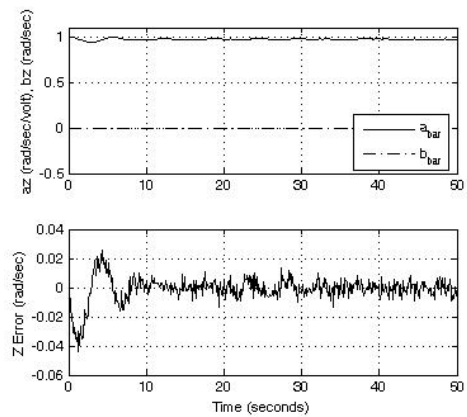
Figure 3.8: Adaptive identifier simulation, path 5 convergence.



(d) Roll parameter convergence, path 7.



(e) Pitch parameter convergence, path 7.



(f) Yaw parameter convergence, path 7.

Figure 3.9: Adaptive identifier simulation, path 7 convergence.

Figures (3.6) through (3.9) illustrate that the parameters converge. Tables 3.2 through 3.4 contain the coefficient estimations generated by the adaptive identifier algorithm for the eight different AUV trajectories. The paths with the lowest level of gyroscope excitation resulted in the worst coefficient estimations, whereas the paths with higher levels of excitation produced better estimates.

Table 3.2: Adaptive identifier simulation results, X gyroscope.

Path	Coef. Estimate		% Error	
	\bar{a}	\bar{b}	\bar{a}	\bar{b}
1	0.9192	0.0919	1.12%	1.04%
2	0.9109	0.0911	0.19%	0.16%
3	0.9112	0.0911	0.23%	0.16%
4	0.9137	0.0913	0.51%	0.47%
5	0.9025	0.0906	0.73%	0.35%
6	0.9097	0.0913	0.07%	0.40%
7	0.9933	0.0927	9.26%	1.93%
8	0.9109	0.0911	0.20%	0.21%

The simulation results conclusively indicate that the adaptive algorithm is a promising solution to real-time parameter identification of gyro errors. Convergence to the correct error values is largely dependent on the excitation of the particular axis. When applying this algorithm to real data, the vehicle run will have to have sufficient excitation to cause the parameters to converge to true values.

Table 3.3: Adaptive identifier simulation results, Y gyroscope.

Path	Coef. Estimate		% Error	
	\bar{a}	\bar{b}	\bar{a}	\bar{b}
1	0.9058	-0.0905	0.36%	-0.42%
2	0.9096	-0.0910	0.06%	-0.05%
3	0.9098	-0.0912	0.08%	-0.27%
4	0.9103	-0.0907	0.13%	-0.25%
5	0.9103	-0.0922	0.13%	-1.41%
6	0.9100	-0.0919	0.09%	-1.13%
7	0.8717	-0.0838	4.11%	-7.84%
8	0.9087	-0.0909	0.04%	-0.04%

Table 3.4: Adaptive identifier simulation results, Z gyroscope.

Path	Coef. Estimate		% Error	
	\bar{a}	\bar{b}	\bar{a}	\bar{b}
1	0.9223	-0.0330	17.00%	-70.34%
2	1.0904	-0.1089	1.86%	-2.03%
3	1.0933	-0.1086	1.61%	-2.29%
4	1.0983	-0.1125	1.15%	-1.25%
5	1.0824	-0.1080	2.58%	-2.81%
6	1.0809	-0.1079	2.72%	-2.88%
7	0.9737	-0.0067	12.37%	-93.96%
8	0.8913	-0.0623	19.78%	-43.89%

3.3 Adaptive Identifier Performance on Real Data

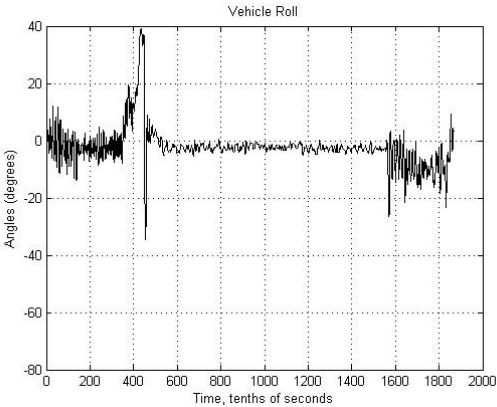
Using data recorded by the ASCL AUV during test runs in Claytor Lake, VA, the adaptive algorithm performance is tested again. One question to be answered with real data is whether the tuning constants, K_η , and Λ must be adjusted depending on the surrounding water dynamics. Performance, such as speed of convergence and damping, will depend largely on the conditions of the environment through which the AUV is running. Claytor Lake has relatively calm water under the surface with slow and constant water currents in a SSW direction.

Two runs are shown here, the first is a straight-line trajectory heading south and the second is a square trajectory. Information regarding each leg of the runs is located in Tables 3.5 and 3.6.

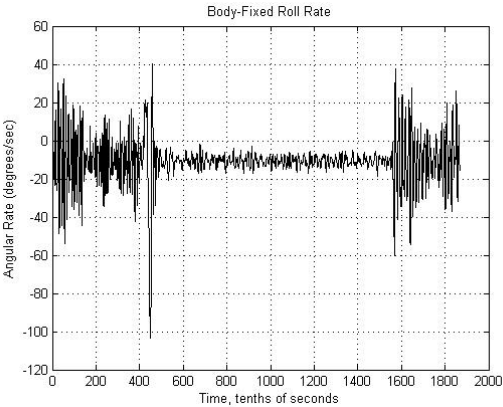
Table 3.5: Commands for straight-line trajectory.

Leg	Heading (deg)	Time(sec)	Depth (m)	Speed (rpm)
1	180	30	0	1200
2	180	120	0.7	1200
3	180	30	0	1200

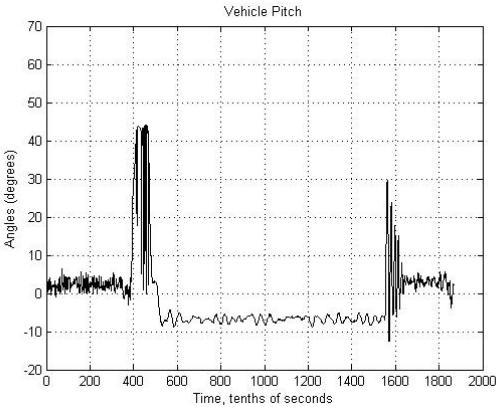
Figures (3.10) and (3.12) show actual data recorded by the AUV while Figures (3.11) and (3.13) display the scale and bias parameter convergence on each axis. From the plots (b), (d), and (f) in Figures (3.10) and (3.12), one can see the difference in driving on the surface from driving underwater. The large oscillations in surface sensor data is due to surface chop and boat wake. For this reason, the adaptive algorithm is not turned on until the AUV enters the underwater portion of the trajectory.



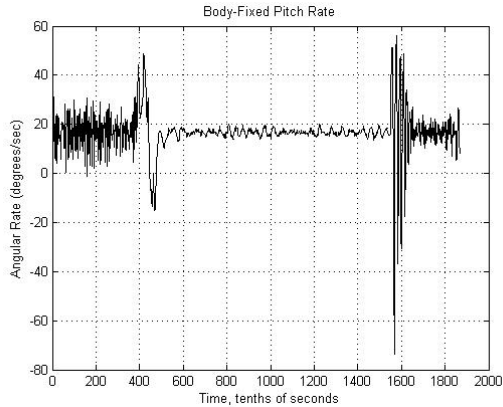
(a) Roll angle data.



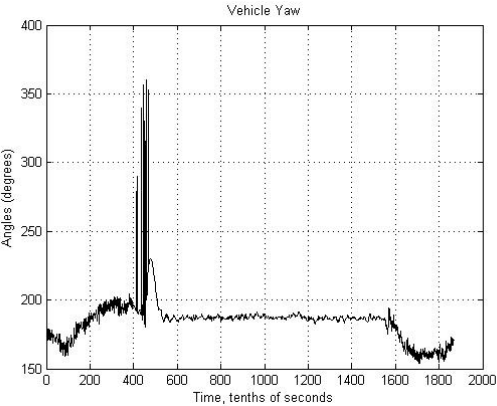
(b) Roll gyroscope data.



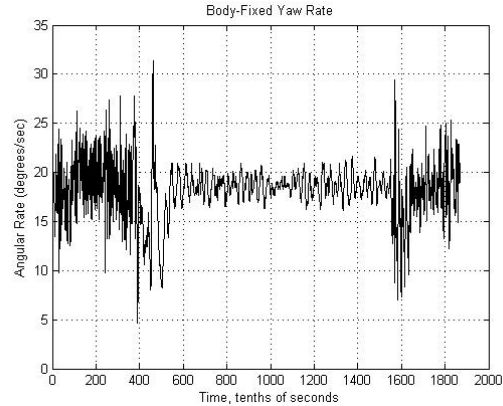
(c) Pitch angle data.



(d) Pitch gyroscope data.

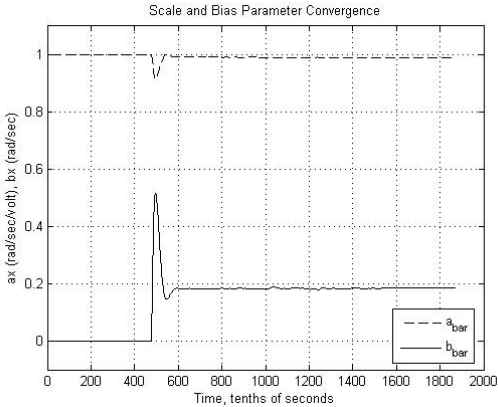


(e) Yaw angle data.

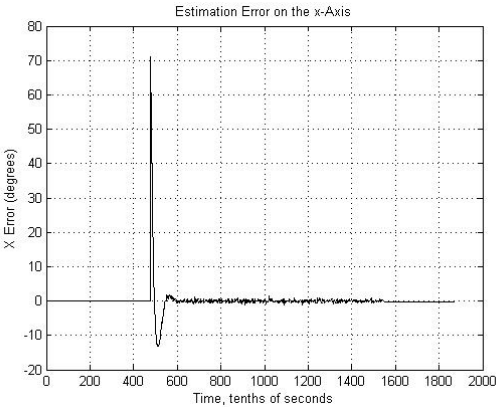


(f) Yaw gyroscope data.

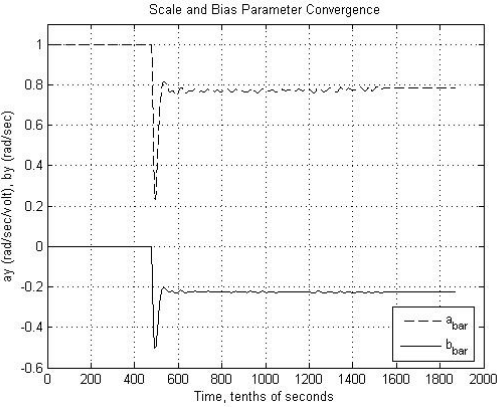
Figure 3.10: Straight-line trajectory sensor data.



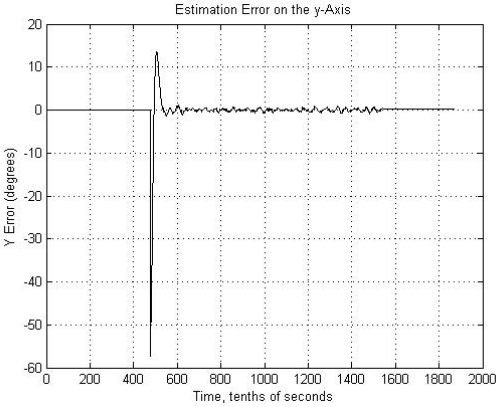
(a) Roll parameter convergence.



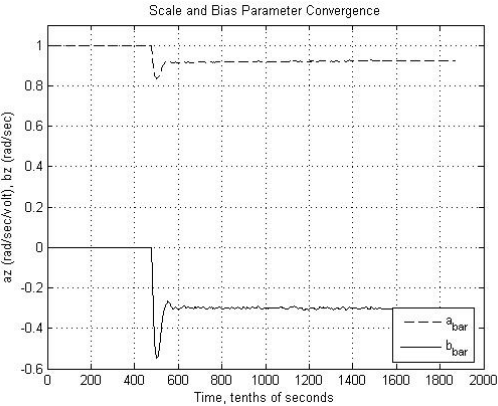
(b) Roll error, $\hat{\phi}(t)$.



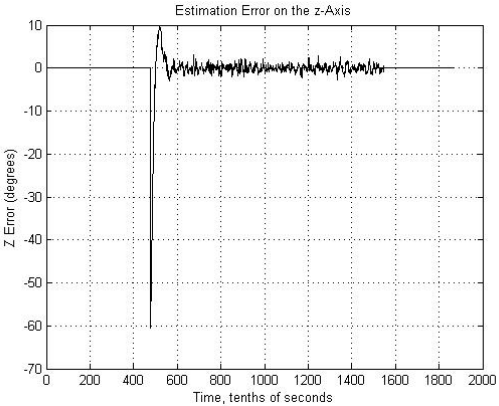
(c) Pitch parameter convergence.



(d) Pitch error, $\hat{\theta}(t)$.

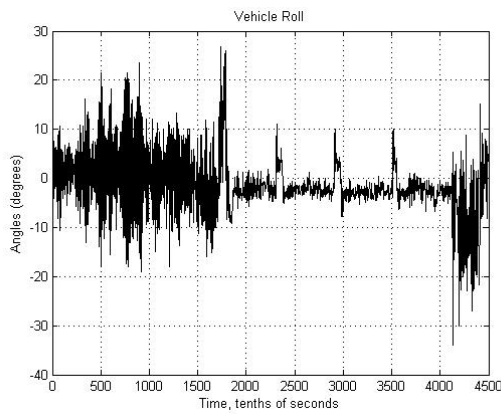


(e) Yaw parameter convergence.

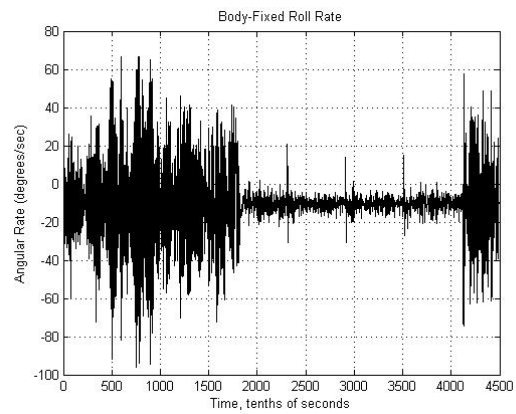


(f) Yaw error, $\hat{\psi}(t)$.

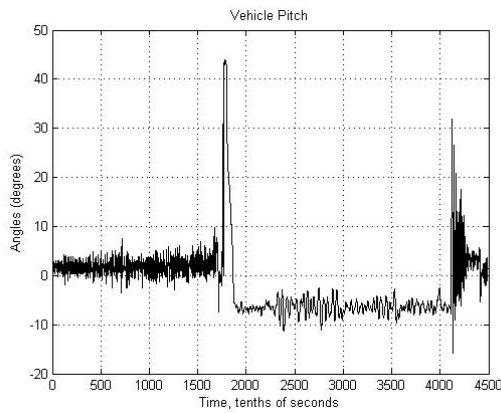
Figure 3.11: Straight-line parameter convergence.



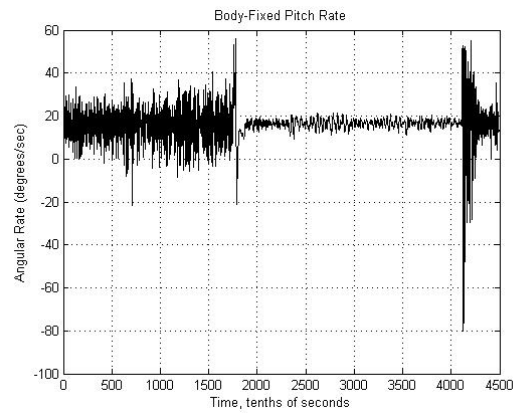
(a) Roll angle data.



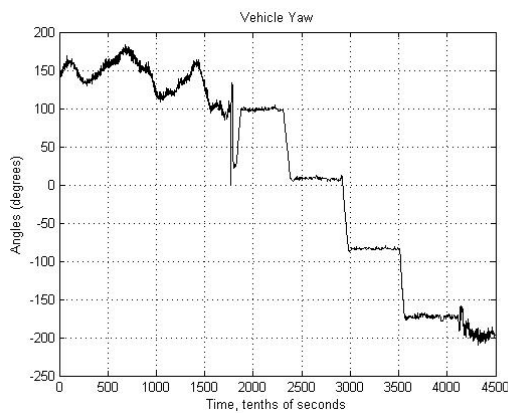
(b) Roll gyroscope data.



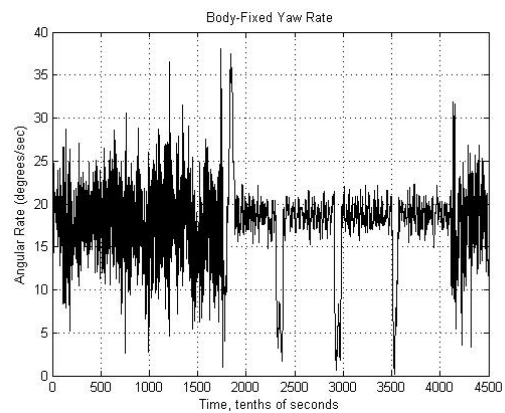
(c) Pitch angle data.



(d) Pitch gyroscope data.

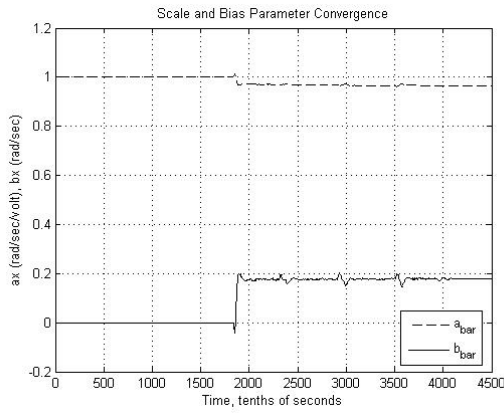


(e) Yaw angle data.

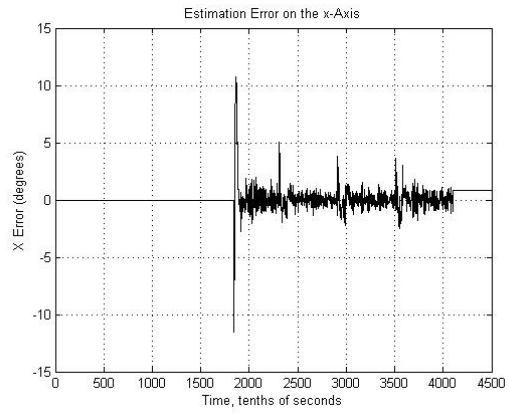


(f) Yaw gyroscope data.

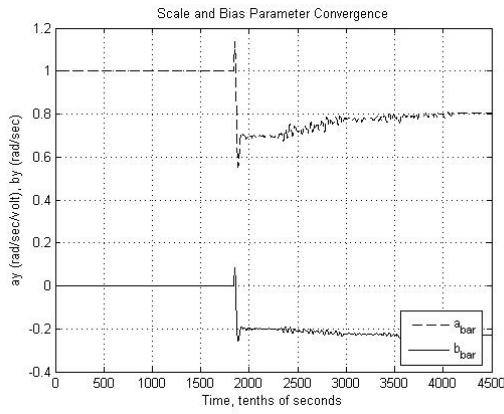
Figure 3.12: Square trajectory sensor data.



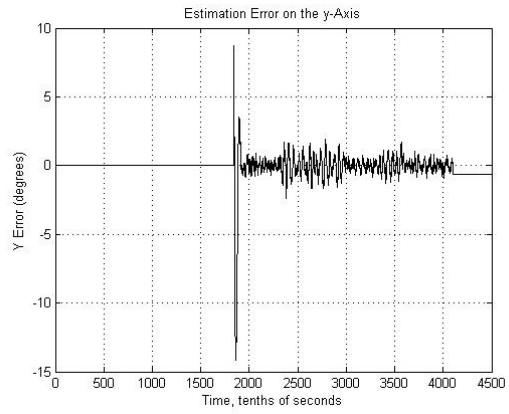
(a) Roll parameter convergence.



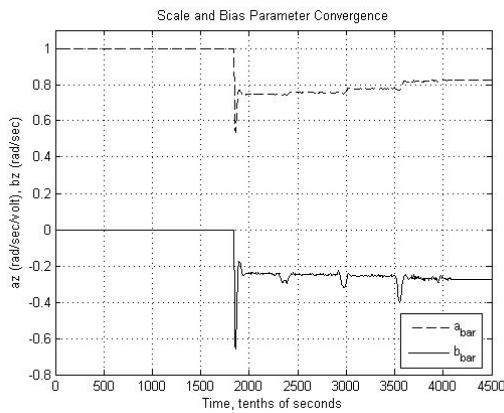
(b) Roll error, $\hat{\phi}(t)$.



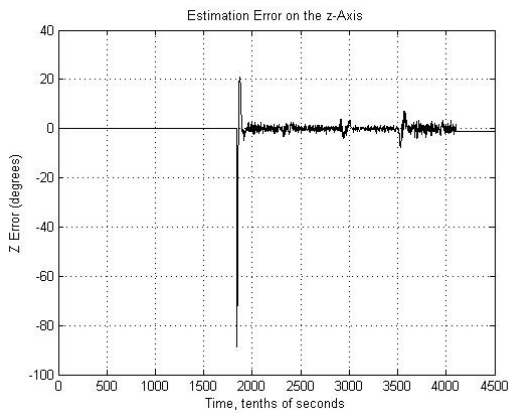
(c) Pitch parameter convergence.



(d) Pitch error, $\hat{\theta}(t)$.



(e) Yaw parameter convergence.



(f) Yaw error, $\hat{\psi}(t)$.

Figure 3.13: Square parameter convergence.

Table 3.6: Commands for square trajectory.

Leg	Heading (deg)	Time(sec)	Depth (m)	Speed (rpm)
1	90	30	0	1200
2	90	60	0.7	1200
3	0	60	0.7	1200
4	270	60	0.7	1200
5	180	60	0.7	1200
6	180	30	0	1200

3.3.1 Calibration Considerations

Unlike simulated data where parameter convergence occurs for nearly all reasonable choices for tuning gains, real data is less clean and requires extensive tuning to achieve desired convergence behaviors. Experience has shown that parameter convergence is not only dependent on the tuning gains but also on the initial conditions in the system. With careful tuning, it has been observed that this dependence can be decreased significantly but not entirely removed.

Through a trial and error approach, the tuning gains are set to

$$\Lambda = \begin{bmatrix} 0.6 & 0 & 0 & 0 & 0 & 0 \\ 0 & 0.55 & 0 & 0 & 0 & 0 \\ 0 & 0 & 5.0 & 0 & 0 & 0 \\ 0 & 0 & 0 & 0.6 & 0 & 0 \\ 0 & 0 & 0 & 0 & 0.7 & 0 \\ 0 & 0 & 0 & 0 & 0 & 0.6 \end{bmatrix} \quad (3.39)$$

and $K_\phi = -1$, $K_\theta = -1$, and $K_\psi = -1$. While the ideal solution is to tune specifically for each vehicle run, the time commitment required makes this option not feasible. Referring to

Figure (3.13c) we can see that the parameters did not converge immediately, which illustrates the lack of optimality of the gain values chosen.

Figure (3.13e) shows the convergence of the yaw rate gyro parameters. After each turn, the parameters converged to different values. This observation shows that this axis does not have sufficient persistence of excitation to converge at once. Only in the turns is this axis excited enough to converge but during the straight portions of the trajectory the parameters cannot converge. In general, the pitch and roll axes do not experience this problem since the AUV rolls and pitches a few degrees consistently throughout the vehicle run. To remedy the lack of excitation on the yaw axis, a specific vehicle trajectory needs to be designed which will guarantee excitation on the yaw axis to allow for accurate parameter convergence. Such a trajectory will give confidence that all parameters have converged to their true values.

Chapter 4

Dead Reckoning

The Extended Kalman Filter (EKF) provides a solution for handling noisy measurements in a noisy system. It provides a unique method that is particularly useful in navigation algorithms to take advantage of the gyroscope's short-term stability and the compass and tilt sensors' long-term reliability. By taking two sensors and fusing their data by means of a Kalman filter, one can obtain the optimal mixing between measurements. Data mixing is also useful when intermittent GPS is available to provide occasional ground truth to the estimated position.

4.1 Extended Kalman Filter

4.1.1 Problem Setup

A detailed description of the EKF is given in [8] and [15]. A brief overview is provided here. The EKF is a means of estimating the state vector, $x \in \mathbb{R}^n$, of a nonlinear system governed

by the following nonlinear difference equation

$$x_k = f(x_{k-1}, u_{k-1}, w_{k-1}) \quad (4.1)$$

with a measurement vector, $z_k \in \mathbb{R}^m$, described by

$$z_k = h(x_k, v_k) \quad (4.2)$$

where u_{k-1} is the system input vector and w_k and v_k are process and measurement noise with covariances, Q_k and R_k , respectively. The system must be linearized by taking the jacobian of the state and measurement equations,

$$A_k = \frac{\partial f}{\partial x}(\hat{x}_{k-1}, u_{k-1}, 0) \quad (4.3)$$

$$B_k = \frac{\partial f}{\partial u}(\hat{x}_{k-1}, u_{k-1}, 0) \quad (4.4)$$

$$H_k = \frac{\partial h}{\partial x}(\hat{x}_k, 0) \quad (4.5)$$

where \hat{x}_k is an estimation of the state vector. Using the linearized system, the EKF is implemented in a recursive two-step process

Prediction Stage

$$\hat{x}_{k|k-1} = f(\hat{x}_{k-1}, u_{k-1}, 0) \quad (4.6)$$

$$P_{k|k-1} = A_k P_{k-1} A_k^T + B_k \Gamma_{k-1} B_k^T + Q_{k-1} \quad (4.7)$$

Correction Stage

$$K_k = P_{k|k-1} H_k^T (H_k P_{k|k-1} H_k^T + R_k)^{-1} \quad (4.8)$$

$$\hat{x}_k = \hat{x}_{k|k-1} + K_k (z_k - h(\hat{x}_{k|k-1}, 0)) \quad (4.9)$$

$$P_k = (I - K_k H_k) P_{k|k-1} \quad (4.10)$$

where Γ_k is the noise covariance associated with the input vector and K_k is the Kalman gain matrix. One must keep in mind that global system properties such as observability are lost in the linearized system estimation.

4.2 Applying the Extended Kalman Filter

Applying the EKF to the ASCL AUV system dynamics is a straightforward application of the vehicle's kinematic model for angular position and the gyro plant model for angular velocity. Inputs into the system are GPS and angular rates. The state vector, s_k is defined as

$$s_k = \begin{bmatrix} x_k & y_k & z_k & \phi_k & \theta_k & \psi_k \end{bmatrix}^T \quad (4.11)$$

and the input vector is

$$u_k = \begin{bmatrix} \omega_{\phi,k} & \omega_{\theta,k} & \omega_{\psi,k} \end{bmatrix}^T. \quad (4.12)$$

The states are updated, when available, with x and y measurements from GPS, z from the depth sensor, and the roll, pitch, and yaw angles measured by the compass. In discrete time, the kinematic and gyro plant models describing the state space system is.

$$\begin{bmatrix} x_k \\ y_k \\ z_k \\ \phi_k \\ \theta_k \\ \psi_k \end{bmatrix} = \begin{bmatrix} x_{k-1} \\ y_{k-1} \\ z_{k-1} \\ \phi_{k-1} \\ \theta_{k-1} \\ \psi_{k-1} \end{bmatrix} + h \begin{bmatrix} V \cos \psi_{k-1} \cos \theta_{k-1} \\ V \sin \psi_{k-1} \cos \theta_{k-1} \\ -V \sin \theta_{k-1} \\ \omega_{x,k-1} + \sin \phi_{k-1} \tan \theta_{k-1} \omega_{y,k-1} + \cos \phi_{k-1} \tan \theta_{k-1} \omega_{z,k-1} \\ \cos \phi_{k-1} \omega_{y,k-1} - \sin \phi_{k-1} \omega_{z,k-1} \\ \frac{\sin \phi_{k-1}}{\cos \theta_{k-1}} \omega_{y,k-1} + \frac{\cos \phi_{k-1}}{\cos \theta_{k-1}} \omega_{z,k-1} \end{bmatrix} \quad (4.13)$$

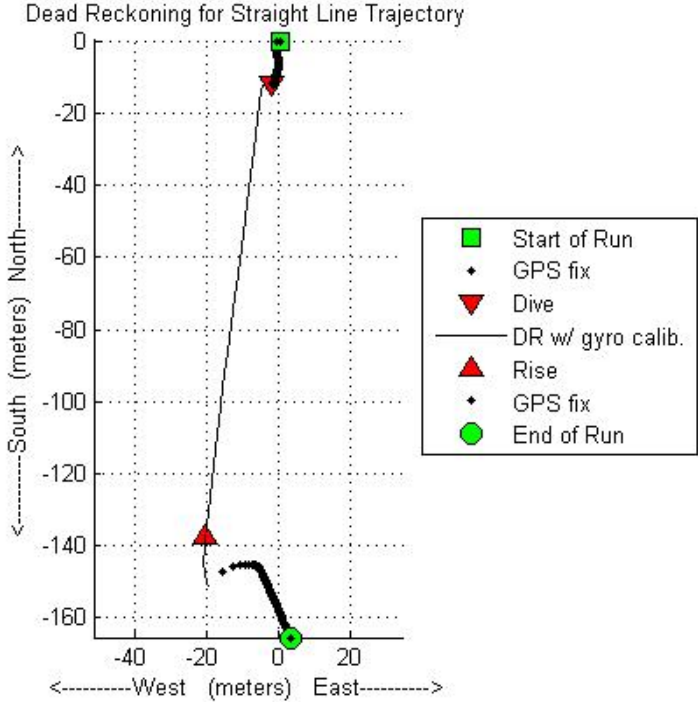
Here, V represents the linear velocity of the AUV in the body-fixed positive x-direction, which is experimentally determined from field experiments. Before the algorithm is applied, A , B , and H , are calculated from (4.3) and (4.4). Since the system model does not change during operation, the linearized system matrices are used directly in the EKF.

The covariance matrices, Q and R , are determined by a method similar to the tuning of the adaptive filter gains. For this system, the value of R is tuned such that when the AUV is on the surface of the water, GPS is trusted almost exclusively. When the AUV dives below the surface, the inertial measurements are trusted exclusively. Thus, during underwater travel the states, x and y , are only estimations of the vehicle position since GPS is not available for the correction stage.

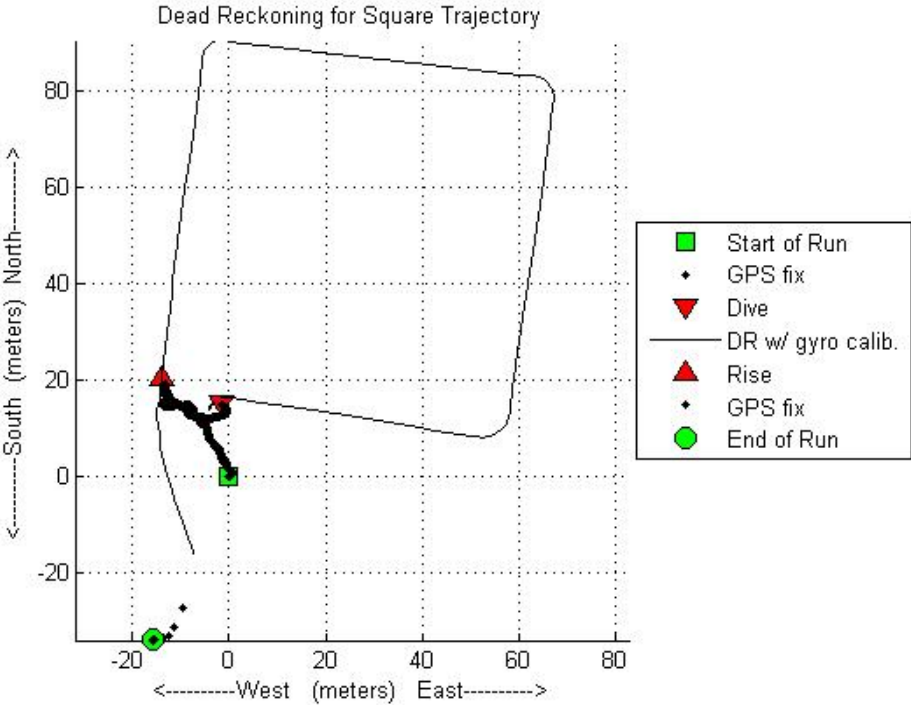
Since the model used to describe the motion of the AUV is kinematic, vehicle dynamics are ignored. During complex turning maneuvers such as diving, rising, and turning, this approximation is especially poor, generating large errors in the estimated position. Increasing Q to add system noise provides enough error to estimate the errors caused by the angle of attack.

4.3 Results

The 6 six state EKF from section 4.2 is applied to the straight-line and the square trajectories analyzed in Chapter 3. Figure (4.1) shows that the EKF does an excellent job estimating the basic shape of the trajectories. It becomes clear that there is an error in the heading measurements though. The compass is known to have an offset. Also, the heading control on the AUV is only a proportional controller making convergence to the commanded heading difficult. Further, the kinematic model does not account for the effects of currents in the water. All these error sources contribute to the error between dead reckoning and GPS



(a) Straight-line trajectory position estimation.



(b) Square trajectory position estimation.

Figure 4.1: Dead Reckoning of the straight-line and square trajectories.

positioning. With these observations in mind, the effects of gyro calibration are examined.

4.4 Gyro Calibration Effects on Dead Reckoning

We are interested in knowing the benefits that calibrated gyro readings have on the dead reckoning algorithm. Therefore, the EKF is applied to the selected trajectories using both calibrated and uncalibrated gyro data. The resulting position estimations are shown in figures (4.2) and (4.3). The axes have been stretched to make plot details more visible.

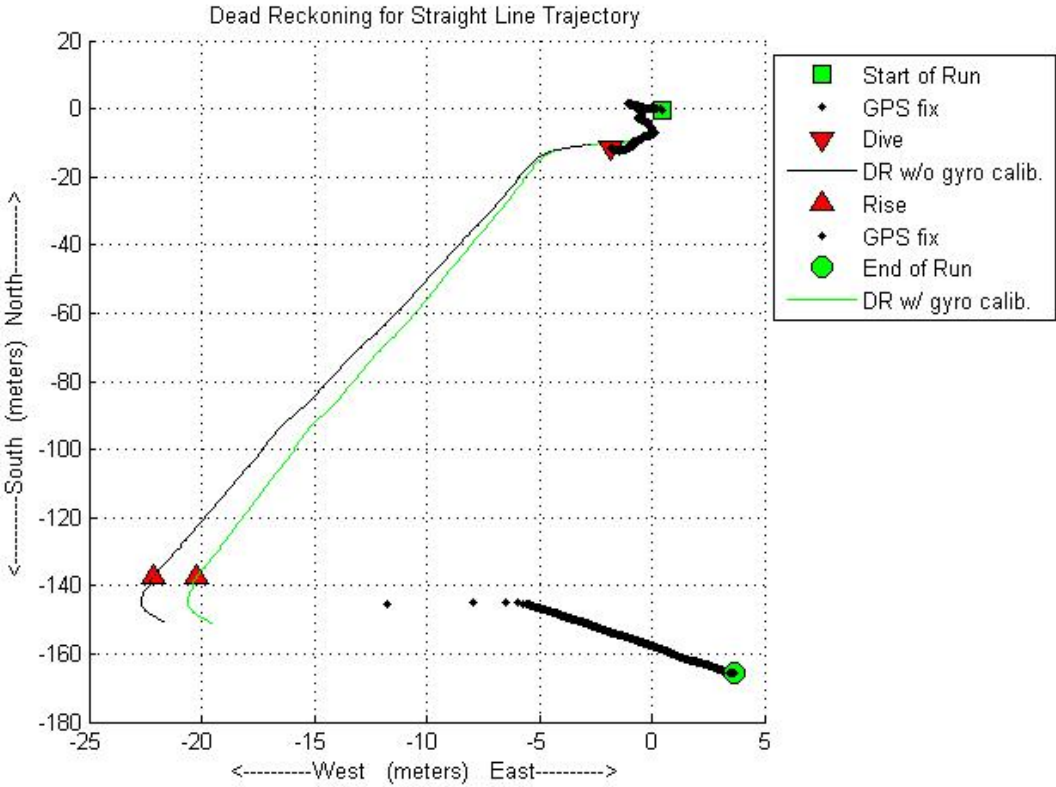


Figure 4.2: Comparison of calibrated vs. uncalibrated gyro on the dead reckoned position for straight-line trajectory.

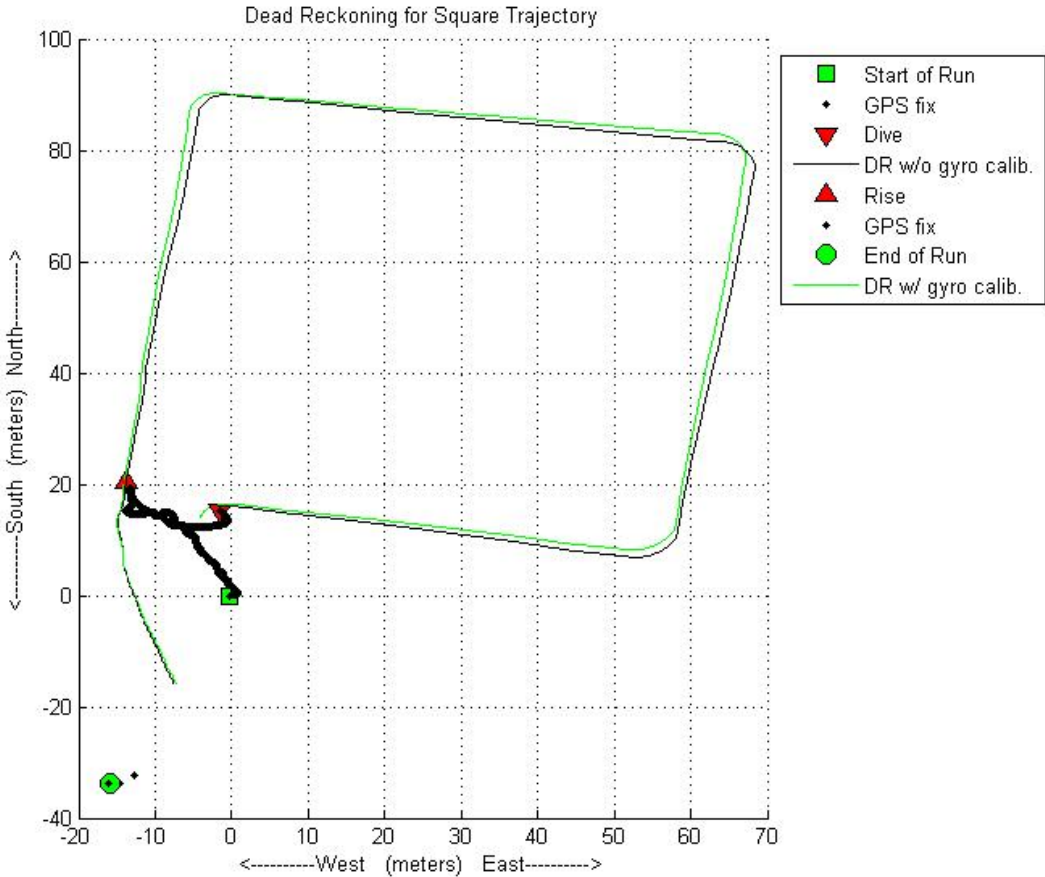


Figure 4.3: Comparison of calibrated vs. uncalibrated gyro on the dead reckoned position for square trajectory.

The errors resulting from an uncalibrated gyro are small as is expected on the straight-line trajectory since the error is small, ($\mu = .25^\circ$). However, using the calibrated data, the dead reckoned position estimation moves closer to the GPS signal received upon rising to the surface. The square trajectory is a relatively short run with each leg lasting only 60 seconds. It is therefore, difficult to make any conclusions about the effects of the gyro calibration.

Unfortunately, not many conclusions can be made about gyro calibration effects on dead reckoning without ground truth position data to give insight into the specific sources of dead

reckoning error. When the ASCL receives a Doppler velocity log (DVL) more conclusive results can be presented.

Chapter 5

Conclusions and Future Work

5.1 Conclusions

A real time parameter estimation algorithm as a method to stabilize the dead reckoned position has shown very promising results. The algorithm's ability to adapt to the changing parameter values as the time interval increases is an integral feature that enhances the capabilities of the AUV. Missions with longer bottom times are now a possibility. A greater confidence can be placed in the precision of the gyros, paving the way for more complex trajectories that include a greater variety of maneuvering patterns instead of straight leg patterns with minimal turning.

The dead reckoning routine has shown estimating a vehicle's position with minimal onboard sensors is a possibility. Given the tolerances on the sensors installed on the ASCL AUV, significant room for improvements in the accuracy and confidence of position estimation are still possible and well within reach with minimal support equipment such as external positioning systems.

5.2 Future Work

While the calibration of the gyros has shown excellent results, there is still much room for improvements. Theory to support the convergence of parameter values would assist in the understanding of the algorithm's performance. A method with which to dynamically adjust the tuning matrices based on estimation error will give more freedom to the AUV allowing for calibration in rougher environments.

Position estimation does have a long way to go before becoming a mature and trustworthy algorithm. Many external factors are ignored in the current version of the dead reckoning EKF. Merging position estimation with water current estimation is a first step. Known currents can be added into the state estimator to adjust the position of the AUV at each time step. Further, the EKF can be used to determine offsets in the compass reading based on GPS points before and after straight-line underwater trajectories. By taking numerous heading measurements with this method in varying directions, a least squares approach can be applied to develop a heading offset table to be included as a variable in the EKF. Much testing will be needed to further analyze the many details involved. The work presented in this thesis forms the foundation for vehicle navigation.

Bibliography

- [1] Analog Devices. $\pm 150^\circ/s$ Single Chip Yaw Rate Gyro with Signal Conditioning.
- [2] D. Gebre-Egziabher, J. D. Powelly, and P. K. Enge. Design and performance analysis of a low-cost aided dead reckoning navigation system. *Gyroscopy and Navigation*, 4, 2001.
- [3] A. J. Healy, P. E. An, and D. B. Marco. Online compensation of heading sensor bias for low cost auvs. *Proceedings of the 1998 Workshop on Autonomous Underwater Vehicles*, August 1998.
- [4] Hassan K. Khalil. *Nonlinear Systems*. Prentice Hall, 3 edition, 2002.
- [5] James C. Kinsey and Louis L. Whitcomb. Towards in-situ calibration of gyro and doppler navigation sensors for precision underwater vehicle navigation. *IEEE International Conference on Robotics and Automation*, 4:4016 – 4023, 2002.
- [6] J. J. Leonard, A. A. Bennett, C. M. Smith, and H. J. Feder. Autonomous underwater vehicle navigation. Technical report, Technical Report, Massachusetts Institute of Technology Department of Ocean Engineering, 1998.
- [7] Jared Mach. Toward auto-calibration of navigation sensors for miniature autonomous underwater vehicles. Master's thesis, Virginia Polytechnic Institute and State University, 2003.

- [8] Peter S. Maybeck. *Stochastic Models, Estimation, and Control*, volume 1. Academic Press, Inc., 1979.
- [9] E. Nebot and H. Durrant-Whyte. Initial calibration and alignment of low-cost inertial navigation units for land vehicle applications. *Journal of Robotic Systems*, 16(2):81–92, 1999.
- [10] Wilson J. Rugh. *Linear System Theory*. Prentice Hall, 1996.
- [11] S. Sastry and M. Bodson. *Adaptive Control: Stability, Convergence, and Robustness*. Prentice Hall, 1989.
- [12] David. A. Smallwood and Louis L. Whitcomb. Preliminary experiments in the adaptive identification of dynamically positioned underwater robotic vehicles. *Proceedings of the 2001 IEEE/RSJ International Conference on Intelligent Robots and Systems*, 2001.
- [13] Mark W. Spong and M. Vidyasagar. *Robot Dynamics and Control*. John Wiley and Sons, 1998.
- [14] D. H. Titterton and J. L. Weston. *Strapdown Inertial Navigation Technology*. Peter Peregrinus Ltd. on behalf of the Institution of Electrical Engineers, 1997.
- [15] Greg Welch and Gary Bishop. An introduction to the kalman filter. Technical report, University of North Carolina at Chapel Hill, 2004.